

The Stellar Population And Origin Of The Mysterious High-Latitude Star Forming Cloud CG 12

Konstantin V. Getman¹, Eric D. Feigelson¹, Warrick A. Lawson², Patrick S. Broos¹,
Gordon P. Garmire¹

gkosta@astro.psu.edu

ABSTRACT

The mysterious high galactic latitude cometary globule (CG) CG 12 has been observed with the ACIS detector on board the *Chandra* X-ray Observatory. We detect 128 X-ray sources, of which a half are likely young stars formed within the globule's head. This new population of $\gtrsim 50$ T-Tauri stars and one new embedded protostar is far larger than the previously reported few intermediate-mass and two protostellar members of the cloud. Most of the newly discovered stars have masses $0.2 - 0.7 M_{\odot}$, and $9 - 15\%$ have K -band excesses from inner protoplanetary disks. X-ray properties provide an independent distance estimate consistent with CG 12's unusual location $\gtrsim 200$ pc above the Galactic plane. The star formation efficiency in CG 12 appears to be $15 - 35\%$, far above that seen in other triggered molecular globules. The median photometric age found for the T-Tauri population is ~ 4 Myr with a large spread of $< 1 - 20$ Myr and ongoing star formation in the molecular cores. The stellar age and spatial distributions are inconsistent with a simple radiation driven implosion (RDI) model, and suggest either that CG 12 is an atypically large shocked globule, or it has been subject to several distinct episodes of triggering and ablation. We report a previously unnoticed group of B-type stars northwest of CG 12 which may be the remnants of an OB association which produced multiple supernova explosions that could have shocked and ablated the cloud over a 15-30 Myr period. HD 120958 (B3e), the most luminous member of the group, may be currently driving an RDI shock into the CG 12 cloud.

¹Department of Astronomy & Astrophysics, 525 Davey Laboratory, Pennsylvania State University, University Park PA 16802

²School of Physical, Environmental, and Mathematical Sciences, University of New South Wales, Australian Defence Force Academy, Canberra, ACT 2600, Australia

Subject headings: HII regions - ISM: globules - open clusters and associations: individual (CG 12) - stars: formation - stars: pre-main sequence - X-rays: stars

1. Introduction

Star formation in the Galaxy occurs on all scales from a small globule collapsing into a single star with planetary system to a giant molecular cloud complex forming rich stellar clusters (Elmegreen et al. 2000). Most stars form in gravitationally unbound groups, and many of these are relatively sparse groups with 10 – 100 members and initial surface density $\lesssim 100$ stars/pc² (Clarke et al. 2000). Unbound sparse clusters are difficult to study because their members quickly disperse and are not easily discriminated from the older Galactic field population. X-ray selection is effective here: median X-ray luminosities of pre-main sequence stars are 30 (5) times higher than ZAMS Pleiades-age stars, and 500 (500) times higher than solar neighborhood stars for $M \simeq 1$ (0.3) M_{\odot} stars (Preibisch & Feigelson 2005). X-ray surveys are also effective in identifying young stars which have lost their protoplanetary disks, and thus effectively complement infrared surveys that preferentially select for disk emission (Feigelson et al. 2007). For example, *ROSAT* studies were responsible for locating most known dispersed ~ 10 Myr old stars associated with the TW Hya and η Cha associations (e.g. Webb et al. 1999; Mamajek et al. 2000), while *XMM-Newton* studies are helping to identify ~ 5 Myr old members of the Upper Scorpius association (Argiroffi et al. 2006). *Chandra* exposures resolve substantial pre-main sequence (PMS) populations embedded in cloud cores (e.g., NGC 1333, Getman et al. 2002), in rich clusters (e.g., Orion Nebula cluster, Getman et al. 2005a), and in sparse gravitationally bound multiple systems (Feigelson et al. 2003).

Some progress is being made towards characterizing the population, dynamics, and particularly the protoplanetary disk evolution of stars born in sparse clusters. Megeath et al. (2005) employed *Spitzer* IRAC photometry to detect a 40% disk fraction around late-type members of the 8 Myr old η Cha cluster at $d = 100$ pc. This disk fraction is higher than expected from studies of richer clusters where a 6 Myr maximum lifetime for inner disks was derived by Haisch et al. (2001). This argues against a single dissipation timescale for all environments and all disk radii. *Spitzer* IRS spectroscopy of η Cha stars by Bouwman et al. (2006) show that the dissipation timescale may be a strong function of binarity, with disks lasting longer around single stars.

We report here a new X-ray selected sample of young stars to further these studies. The target is cometary globule CG 12 (= MBM 112) (Hawarden & Brand 1976), a relatively poorly studied small star forming region at high galactic latitude $(l, b) = (316^{\circ}, 21^{\circ})$, which

is producing a sparse unbound cluster of young stars. Shown in Figure 1, the head of CG 12 is the reflection nebula NGC 5367 (= GN 13.54.7) illuminated by the double B4 + B7 star Herschel 4636 (= CD -39°8581) (Herschel 1847). Signs of ongoing star formation include CO molecular cores (van Till et al. 1975; White 1993; Yonekura et al. 1999; Haikala & Olberg 2006), several IRAS sources (White 1993; Bourke et al. 1995a), a bipolar molecular outflow (White 1993), and three stars with K-band excesses (Santos et al. 1998). Optical photometry and spectroscopy of the brightest stars in the region reveal three B type (B4, B7, B8) and two A type (A2 + A4) candidate members (van Till et al. 1975; Williams et al. 1977; Maheswar et al. 2004). The most recent mass estimate for the total of all three molecular cloud cores (CG 12SW, CG 12S, and CG 12N) found in CG 12, ranges from 100 to 250 M_{\odot} with the peak column density through the densest core, CG 12N, of $\sim 2.2 \times 10^{22} \text{ cm}^{-2}$ ($A_V \sim 13 \text{ mag}$) (Haikala & Olberg 2006). Due to its high Galactic latitude, contamination by field stars and obscuration by foreground interstellar matter is much lower than for most star forming regions.

Compact CGs, along with other Bok globules, are interpreted as the last vestiges of the molecular cloud that gave birth to OB stars (Bok & Reilly 1947; Hawarden & Brand 1976). CGs are distributed widely across the Milky Way but are rarely found at high latitude (Bourke et al. 1995a). Most lie within giant HII regions such as IC 2944, the Rosette and Carina nebulae, and most prominently in the huge expanding Gum Nebulae surrounding the Vela OB2 association. CGs are modeled as externally illuminated, photoevaporated and ablated into elongated head-tail morphologies by ultraviolet radiation of OB stars (Reipurth 1983). It is likely that pressure from the ionization shock front at the surface propagates through a globule and overcomes the magnetic, turbulent and thermal pressure that supports it against collapse, thereby triggering star formation. This process of radiation-driven implosion (RDI) in molecular globules was originally studied through analytical models for spherical clouds (Bertoldi 1989) and 2-dimensional hydrodynamical calculations (Lefloch & Lazareff 1994, 1995). Recent 3-dimensional calculations of RDI processes in molecular globules, including self-gravity, heating, and cooling, are presented by Kessel-Deynet & Burkert (2003) and Miao et al. (2006). The characteristic timescale for producing cometary morphologies and inducing gravitational collapse is 0.1 – 0.5 Myr.

Generally, the stellar populations of these isolated triggered star formation regions are poorly known. Some globules show clear evidence for embedded young stars, such as *IRAS* sources, while others do not. $H\alpha$ and *JHK* surveys of bright-rimmed globules containing embedded IRAS sources revealed several cases with small clusters of T Tauri and *K*-band excess stars within and in front of the bright rim (Sugitani et al. 1995; Ogura et al. 2002; Thompson et al. 2004). Molecular outflows and masers are found in several globule cores with IRAS sources (De Vries et al. 2002; Urquhart et al. 2006). Directly supporting the

RDI triggering mechanism, age gradients in the stellar population (where the youngest stars are embedded and older stars are aligned toward the ionizing sources) have been recently reported in irradiated molecular globules within the large IC 1848 and IC 1396 HII regions (Matsuyanagi et al. 2006; Ogura et al. 2006; Getman et al. 2007). For example, our *Chandra/Spitzer* study of IC 1396N revealed a spatial-age gradient in the globule from Class III to Class I/0 among 25 young objects (Getman et al. 2007).

The existence of any star forming dark cloud at Galactic location $(l, b) = (316^\circ, 21^\circ)$ is unusual, and the cometary structure of CG 12 in such an isolated environment is even more mysterious. There are no reported luminous OB-type stars at even higher latitudes to produce the head-tail morphology with its tail pointing towards (not away from) the Galactic plane. The origin of CG 12 is thus uncertain. Williams et al. (1977) suggested that a high latitude supernova explosion ($l \simeq 320^\circ, b \simeq 30^\circ$) could have ablated the cloud and triggered star formation. We develop these ideas here and identify a specific stellar group which may be responsible for compressing and ablating the CG 12 cloud.

The CG 12 population is likely to be far larger than that of previously studied molecular globules. The presence of five intermediate-mass ($2 < M < 7 M_\odot$) B4-A4 stars (Williams et al. 1977; Maheswar et al. 2004) demands the presence of ~ 30 stars with masses $0.5 < M < 2 M_\odot$ and ~ 50 stars with masses $0.2 < M < 0.5 M_\odot$, assuming a Galactic field Initial Mass Function (Kroupa 2002). Thus, roughly a hundred cloud members are expected to be present. A fraction of these stars have already been detected in X-rays, although the result has not been published. An archived 9 ks *ROSAT*-PSPC image (obtained to study shadowing of the soft X-ray background by CG 12) harbors ~ 30 soft X-ray sources within the globule’s head and in the arc around the globule (Figure 2). Most of those are clearly not background sources, as the remainder of the *ROSAT* field is nearly empty. CG 12 thus appears to be the most active star forming center among the known cometary globules, and should provide a valuable laboratory for testing theories of triggered star formation.

This paper begins a study of the CG 12 stellar population based on an X-ray survey designed to address the issues outlined above. We discuss the population, spatial and age distribution, dynamics, and star formation history. We suggest how a CG morphology arose at this atypical isolated location. Our work is based on a mosaic of four images obtained with the *Chandra* X-ray Observatory combined with published optical, infrared and radio data. With its excellent mirrors and detectors, *Chandra* achieves an order-of-magnitude improvement in sensitivity and spatial resolution compared to *ROSAT*. Our planned new optical and *Spitzer*-IRAC studies of the CG 12 stellar population will be described in subsequent papers.

The *Chandra* observations of CG 12 and source list are described in §2, optical and

near-infrared (ONIR) counterparts to *Chandra* sources are presented in §3, and evaluation of X-ray contaminants unrelated to the cloud is provided in §4. The X-ray and ONIR properties of most of the discovered T-Tauri stars with a preliminary analysis of their disks and kinematics are reported in §2.3 and 5. Discussion of the distance to CG 12 is presented in §6. The inferred global properties of the CG 12 stellar population, including its age distribution, star formation efficiency, and spatial structure appear in §7. We end in §8 with a discussion of the new observational findings and their implications for the history of star formation and origin of CG 12.

2. The *Chandra* Observations and Analysis

2.1. Observation and Data Reduction

The current project combines four X-ray observations of the globule, one primary field (I in Fig. 1) with ~ 31 ks exposure directed at the globule’s core and three secondary fields (II, III, and IV in Fig. 1) with ~ 3 ks exposures positioned contiguously to the north and west of the core. The primary pointing is intended to detect the population of pre-main sequence stars forming in the molecular head of the globule. The secondary pointings are designed to locate an older population of stars expected if the present cloud is only the ablated remnant of a larger cloud that experienced sequential star formation triggering events, similar to the sequence of stars found in our *Chandra* study of IC 1396N (Getman et al. 2007).

The observations were obtained with the ACIS camera (Garmire et al. 2003) on-board *Chandra* (Weisskopf et al. 2002) as described in Table 1. For each observation we consider here only results arising from the imaging array (ACIS-I) of four abutted 1024×1024 pixel front-side illuminated charge-coupled devices (CCDs) covering about $17' \times 17'$ on the sky. The S2 and S3 detectors in the spectroscopic array (ACIS-S) were also operational, but as the telescope point spread function (PSF) is considerably degraded far off-axis, the S2-S3 data are omitted from the analysis. All four observations were performed during a quiet phase of solar activity; no background flares due to particle contamination were encountered.

Data reduction follows procedures similar to those described in detail by Townsley et al. (2003, Appendix B) and Getman et al. (2005a). Briefly, the data are partially corrected for CCD charge transfer inefficiency (Townsley et al. 2002), selected by event “grade” (only ASCA grades 0, 2, 3, 4, and 6 are accepted), “status”, and “good-time interval” filters, trimmed of background events outside of the 0.5 – 8.0 keV band, and cleaned of hot pixel columns with energies of < 0.7 keV left by the standard processing. The slight PSF broadening from the *Chandra* X-ray Center’s (CXC’s) software randomization of positions is re-

moved. Based on several dozen matches between bright *Chandra* and 2MASS point sources, we applied a small astrometric correction to source positions to place the absolute astrometry to the *Hipparcos* reference frame. These and later procedures were performed with *CIAO* software package 3.3, *CALDB* 3.2.1, *HEASOFT* 6.1.1, CTI corrector version 1.44, and the *ACIS Extract* package version 3.94. The latter two tools were developed at Penn State and are publicly available¹.

2.2. X-ray Point Source Catalog

Figure 3 shows the resulting image of the ACIS-I field after adaptive smoothing with the *CIAO* tool *csmooth*. More than 100 point sources are easily discerned. Source searching was performed with data images and exposure maps constructed at three spatial resolutions (0.5, 1.0, and 1.4'' per pixel) using the *CIAO wavdetect* tool. We run *wavdetect* with a low threshold $P = 10^{-5}$ which is highly sensitive but permits false detections at this point in the analysis. This is followed by visual examination to locate other candidate sources, mainly close doubles and candidate sources near the detection threshold. Using *ACIS Extract*, photons are extracted within polygonal contours of $\sim 90\%$ encircled energy using position-dependent models of the PSF.

Background is measured locally in source-free regions. Due to the very low, spatially invariant, ACIS-I background in the *Chandra* observations of CG 12 there is a one-to-one correspondence between a source’s significance and net counts (a similar correspondence is seen in the *Chandra* data of IC 1396 globule, see Figure 2 of Getman et al. 2007). This uniform background is much simpler than in the *Chandra* Orion Ultradeep Project (COUP) observation of the Orion Nebula Cluster where source crowding, readout trails and PSF wings from bright sources complicate the analysis (Getman et al. 2005a). The source significance calculated by *ACIS Extract* is the ratio of the source’s net (background-subtracted) counts to the uncertainty on that quantity²: $Signif = NetFull/\sigma(NetFull)$. Following the procedure of Getman et al. (2007), the list of candidate sources is trimmed to omit sources with fewer

¹Descriptions and codes for CTI correction and *ACIS Extract* can be found at <http://www.astro.psu.edu/users/townsley/cti/> and http://www.astro.psu.edu/xray/docs/TARA/ae_users_guide.html, respectively.

²The uncertainty on the net counts is estimated by calculating errors (Gehrels 1986, eqs. 7 and 12) on total observed and background counts and then propagating (Lyons 1991, eq. 1.31) those errors to net counts. More detailed information on the algorithm for calculating source significance can be found in the section “Algorithms”, subsection “Broad Band Photometry”, of the Users Guide for *ACIS Extract* at http://www.astro.psu.edu/xray/docs/TARA/ae_users_guide.html.

than ~ 5 estimated source net counts, $NetFull/PSFfrac \lesssim 4.5$. In the case of CG 12 observations the above criterion is equivalent to accepting sources with a source significance of $Signif \gtrsim 1.1$. The resulting catalog of 128 sources is listed in Table 2.

The *ACIS Extract* package estimates (often using *CIAO* tools) a variety of source characteristics including celestial position, off-axis angle, net and background counts within the PSF-based extraction area, source significance assuming Poisson statistics, effective exposure (corrected for telescope vignetting and satellite dithering), median energy after background subtraction³, a variability indicator derived from the one-sided Kolmogorov-Smirnov statistic, and occasional anomalies related to chip gap or field edge positions. These are all reported in Table 2; see Getman et al. (2005a) for a full description of these quantities.

Figure 4 summarizes extracted properties of the 128 *Chandra* point sources in four dimensions: source position on the sky, median energy of the source photons, and count rate. The three known B-type members of the region are detected by *Chandra* (§7.1). These are *Chandra* sources L_57, L_58, and L_74. Most of the unabsorbed X-ray point sources (red circles in Figure 4) are likely previously unreported T-Tauri stars formed in the cloud (§4, 5, and 7.2). Several bright hard X-ray sources (large blue circles) coincide with the C¹⁸O molecular cores of Haikala & Olberg (2006): L_45 and L_46 lie within CG 12N, and L_54 lies within CG 12S. These are probably embedded protostars (§5 and 7.3). Most of the remaining X-ray sources (small cyan and blue circles) have no stellar counterparts; many of these should be extragalactic contaminants (§4).

2.3. X-ray spectral analysis

For *Chandra* sources with > 20 net counts, we performed spectral analysis with the *XSPEC* spectral fitting package version 12.2 (Arnaud 1996). The unbinned source and background spectra were fitted with one-temperature APEC plasma emission models (Smith et al. 2001) using the maximum likelihood method which is believed to be well suited to low-count sources (Cash 1979). We assumed 0.3 times solar elemental abundances previously suggested as typical for young stellar objects in other star forming regions (Imanishi, Koyama, & Tsuboi 2001; Feigelson et al. 2002). Solar abundances were taken from Anders & Grevesse (1989). X-ray absorption was modeled using the atomic cross sections of Morrison & McCammon (1983).

Best-fit plasma parameters inferred from our spectral fits and derived broadband lumi-

³The derivation of median energy of background-subtracted events is given in Townsley et al. (2006, §3.1).

nosities are tabulated in Table 3. See table notes for further details. The derived parameters are generally consistent with the correlation between the absorbing column density and photometric source median energy ($MedE$) found for Orion stars in our COUP study (see Figure 8 in Feigelson et al. 2005). In several cases where the source is not truly associated with a CG 12 star (§4), source luminosities reported in Table 3 are obviously wrong. For instance, hard X-ray source L_2 outside of the molecular cloud is a good extragalactic candidate, while an extremely soft X-ray source L_81 is likely to be a foreground star (§4).

3. ONIR counterparts

Chandra source positions were compared with source positions from three ONIR catalogs. The Naval Observatory Merged Astrometric Dataset (NOMAD; Zacharias et al. 2004a) contains astrometric and photometric data for over 1 billion stars derived from the Hipparcos, Tycho-2, UCAC2, and USNO-B catalogs. A list of stars around CG 12 with *BVRI* photometry is provided by Maheswar et al. (2004). The Two Micron All-Sky Survey (2MASS; Cutri et al. 2003) catalog gives sources down to $K \sim 15.5$ mag. *Chandra* sources were considered to have stellar counterparts when the positional coincidences were better than $1''$ within $\sim 3.5'$ of ACIS-I field center, and $2''$ in the outer regions of each ACIS-I field where *Chandra* PSF deteriorates. *Chandra*-2MASS (*Chandra*-NOMAD) median offsets are better than $0.2''$ ($0.3''$) at the central part of the field and $0.4''$ ($0.5''$) at larger off-axis angles, which are similar to those found in the COUP observation (Getman et al. 2005a). We find that NOMAD is slightly more sensitive than 2MASS catalog for *Chandra* counterparts: 55 (out of 128) X-ray sources have optical counterparts while 47 have 2MASS counterparts. All five with optical but without 2MASS counterparts are faint with $R \sim 19$ mag sources; some of these may be extragalactic.

Individual ONIR counterparts for *Chandra* sources are listed in Table 4 along with their optical *VR* and NIR *JHK_s* magnitudes and proper motions. See table notes for details. When an optical counterpart from Maheswar et al. (2004) is present, its more reliable CCD photometry supersedes the photographic photometry from the NOMAD catalog.

We established in our COUP study of Orion stars that the X-ray median energy, $MedE$, of a PMS star is an excellent surrogate for its line-of-sight obscuration, N_H (Feigelson et al. 2005). Figure 5 examines the relationship between the presence of an optical counterpart, the X-ray count rate, and X-ray median energy derived from the X-ray photometry (Table 2). The presence of optical counterparts correlates well with low median energy ($MedE < 2$ keV corresponding to $\log N_H < 22.0 \text{ cm}^{-2}$), but shows little relation to the count rate. From this figure, we roughly partition the *Chandra* sources into three groups which are discriminated

by symbol color in Figure 4:

1. Group 1 consists of the 42 unobscured or lightly obscured sources with $MedE \leq 1.4$ keV (red circles in Figure 4) of which 88% are identified with ONIR sources down to $R \sim 19$ mag. All 27 of these sources from field I have optical counterparts. In fields II-IV, 5 out of 15 sources lack optical counterparts (II_4, III_3, IV_4, IV_5 and IV_9).
2. Group 2 consists of 54 lightly-moderately and some heavily obscured *Chandra* sources with $1.4 < MedE \leq 2.5$ keV (orange, green, and cyan objects in Figure 4). Only 28% of these sources are identified with ONIR counterparts.
3. Group 3 consists of the 32 heavily obscured sources or intrinsically hard X-ray sources with $MedE > 2.5$ keV (blue objects in Figure 4). Only 9% of these sources have been identified in ONIR bands.

To facilitate later photometric study, we have calibrated the photographic R -band magnitudes obtained from the NOMAD catalog to the more accurate CCD magnitudes of Maheswar et al. (2004). For stars in both samples, we find that USNO-B R -band magnitudes from NOMAD catalog are systematically overestimated by ~ 0.5 mag and can be mostly corrected by the linear correction $R_{NOMAD,c} = 1.03 \times R_{NOMAD} - 0.92$. Figure 6 compares the corrected NOMAD and CCD magnitudes. From the figure, we see that the NOMAD values are about 0.2 mag too faint for $R \gtrsim 16.2$ mag. With these additional corrections, the formal 1σ errors for R -band magnitudes are better than ~ 0.2 mag for all *Chandra* counterparts with $R > 12$ mag.

4. Sources unrelated to the cloud

Unlike in the highly concentrated ONC cluster in the COUP observation, a significant fraction of X-ray sources in *Chandra* observations of sparse clusters are unrelated to the star forming region. To quantify this contamination, we performed detailed Monte-Carlo simulations of Galactic field and extragalactic background contamination populations as described in Getman et al. (2005b, 2006).

The Galactic field contamination is estimated from simulations of Galactic stellar populations by Robin et al. (2003), henceforth the Besançon model⁴. We convolve the simulated stellar population in a *Chandra* field at $(l, b) = (316.5, +21.1)$ with the X-ray luminosity

⁴Simulations are provided at <http://bison.obs-besancon.fr/modele/>.

functions of normal Galactic disk stars in the solar neighborhood measured from *ROSAT* surveys (Schmitt et al. 1995; Schmitt 1997; Hünsch et al. 1999) and then apply the observational limit of our *Chandra* observations. The Besançon model predicts ~ 100 foreground stars (74% M, 10% K, 10% G, and 6% F dwarfs) mostly at distances of 250 – 550 pc with one third having ages < 3 Gyr. It predicts ~ 2700 background stars down to $V < 22$ mag (18% M, 34% K, 28% G, 18% F dwarfs, and 2% giants) mostly at distances of 0.6 – 10 kpc with > 3 Gyr ages.

Convolving these distributions with the *ROSAT* luminosity functions, and including the effect of spatially-dependent absorption derived from the $C^{18}O$ column map of Haikala & Olberg (2006) (assuming a correspondence of 0.3 K km/s to $A_V \sim 1$ mag), we obtain a predicted X-ray source contamination in the *Chandra* field I of ~ 4 M and ~ 1 G-F dwarfs at distances around 300 pc. Source I_81 is very likely one of these contaminants; it has a very soft X-ray spectrum, and has independently been suggested to be a G8–K5 field star unrelated to CG 12 (WBLH #4 in Marraco & Forte 1978; Maheswar et al. 2004). No more than 1 foreground star of a spectral type G or F is expected in each of the secondary *Chandra* fields (II, III, and IV). The simulations predict that $\lesssim 2$ background giants will be present in field I, and no background dwarfs will be detected in any field.

Contamination by extragalactic X-ray sources will be more important. This is evaluated by applying the instrumental background and obscuration effects of the molecular cloud to simulated extragalactic X-ray source populations drawn from the hard band X-ray background $\log N - \log S$ distribution of Moretti et al. (2003). Power-law spectra are assumed consistent with flux-dependencies obtained by Brandt et al. (2001).

For each of the secondary *Chandra* fields, the simulations predict from 4–11 extragalactic contaminants. The best AGN candidates in our secondary fields are those without ONIR counterparts; we see 19 such sources (Table 4) consistent with the simulations. Most have hard band observed X-ray fluxes $\lesssim 10^{-13}$ ergs cm^{-2} s^{-1} and R -band magnitudes > 19 mag, consistent with measured extragalactic X-ray flux- R magnitude dependencies (Barger et al. 2003; Steffen et al. 2004).

The simulations for the primary *Chandra* field predict $\sim 40 - 50$ extragalactic contaminants: around half of the contaminants in the range of low hard-band observed fluxes of $10^{-14.5} - 10^{-14.2}$ ergs cm^{-2} s^{-1} and another half in the brighter range of $> 10^{-14}$ ergs cm^{-2} s^{-1} . This implies that most of the Group 2 and Group 3 sources in the field I are expected to be extragalactic. The assumption of the existence of some number of pre-main sequence stars without optical counterparts⁵ lightly or moderately embedded in the molecular cloud or lo-

⁵For instance, according to theoretical PMS models CG 12 members with $0.2 - 0.5 M_{\odot}$ and ages $\gtrsim 4$ Myr

cated behind it introduces some confusion between the simulated number of extragalactic contaminants and the expected low-mass T-Tauri members of the region from Group 2.

4.1. Counterpart summary

Based on the spatial distribution of *Chandra* sources (Figure 4), the link between optical counterparts and low obscuration (Figure 5), and the results of these simulations of Galactic and extragalactic contaminants in the *Chandra* fields, we thus emerge with the following results. With the exception of a few foreground stellar contaminants, most of the 42 Group 1 sources ($MedE \lesssim 1.4$ keV) are probably lightly-obscured low-mass T-Tauri stars emerged from the CG 12 molecular cloud. With the exception of a few hard X-ray sources spatially coincident with the cores of the molecular cloud (§7.3), most of the 32 Group 3 sources ($MedE > 2.5$ keV) are likely extragalactic background contaminants unrelated to the CG 12. Among the remaining 54 Group 2 sources ($1.4 < MedE < 2.5$ keV), some can be PMS stars embedded in the cloud or located behind it, and some can be extragalactic background contaminants. The 15 of these 54 with ONIR counterparts are very likely to be YSOs. In total, about 60 young stars are X-ray detected, increasing the known population of the cloud by a factor of ~ 10 .

5. ONIR properties of *Chandra* sources

5.1. Color-magnitude and color-color diagrams

Figures 7 and 8 present ONIR properties for most of the *Chandra* sources with ONIR counterparts based on the photometric data in Table 4. The R vs. $R - K$ color magnitude diagram in Figure 7 has 32 *Chandra* sources with R -band magnitudes and high-quality *2MASS* photometry⁶. Two lightly-obscured and two embedded protostellar candidates are added in the $J - H$ vs. $H - K_s$ color-color diagram in Figure 8: I_29, I_44, I_45 and I_46. Several brighter sources with $R < 12$ mag, for which the photographic-CCD photometric

will have $R > 19$ mag (= no optical counterpart), if subject to absorption $A_V > 2$ mag.

⁶We restrict the sample here mostly to *2MASS* sources with AAA photometric flags and 000 confusion flags which have typical JHK_s color errors $\lesssim 0.03$ mag. The quality is lower for four sources: I_57, I_66, I_73, and III_7). JHK_s magnitudes in Figure 8 are in the *2MASS* photometric system, whereas in Figure 7 K_s magnitudes have been transformed to the color system of Bessell & Brett (1988) to be in agreement with R -band magnitudes transformed to the Johnson (1966) system here.

calibration is not known (Figure 6), are also added in Figure 8: I_57, I_70, I_74 and I_81, I_84, II_5 and II_12. PMS evolutionary tracks from the calculations of Siess et al. (2000) are shown in both diagrams; a distance of 550 pc (§6) is assumed for the conversion of absolute to apparent R magnitude in Figure 7.

While accurate classification of the *Chandra* sources must await our upcoming optical spectroscopic measurements, the nature of the sources with known ONIR photometry can be estimated from these diagrams. Most are unreddened or lightly obscured ($A_V < 2$ mag), with positions in the color-magnitude diagram consistent with low-mass $0.2 - 0.7 M_\odot$ PMS stars. A wide spread of ages, ranging from $\lesssim 1$ to ~ 20 Myr, is seen. Although we have not applied any reddening corrections, we believe this result is robust since the reddening vector in the color-magnitude diagram is nearly parallel to the isochrones. No spatial pattern in ages is seen; in particular, we find no indication that stars in the secondary fields are systematically older than the lightly obscured stars in the primary field.

Four stars have JHK colors indicating heavy absorption corresponding to $5 < A_V < 50$ mag: I_29, I_42, I_45, and I_46. The latter two sources and the source I_54 (with no ONIR counterparts) are located towards the molecular cores and are likely members of the younger embedded in the cloud population of CG 12 (§7.3).

One *Chandra* star is unusual in its absorption characteristics. The low $MedE = 1.2$ keV of the *Chandra* source I_29 indicates a low absorbing column density that stands in contrast to the higher $A_V \sim 6$ mag inferred from its JHK_s colors. This may be due to binarity, or to an unusual disk geometry or gas-to-dust ratio. A similar inconsistency between near-infrared colors and X-ray absorption was found for SVS-16 in the NGC-1333 star forming cloud (Getman et al. 2002).

5.2. Inner disk emission

Out of 33 likely low-mass lightly and moderately obscured pre-main sequence stars (not including members of the embedded population, such as I_45, I_46, and high-mass candidate I_57) in the Figure 8 color-color diagram, 3 – 5 (9 – 15%) appear to have K -band excesses: I_29, I_51, I_84, III_2 and possibly I_66. Three of these stars lie on the edges of the molecular cores, and two are far from the cloud (Figure 4). However, the offsets from the locus of reddened photospheres is typically small (~ 0.1 mag), and the K -band offsets may not be statistically significant in all cases. In the other direction, several highly obscured sources (established from their high values of $MedE$) are not seen by *2MASS*, and members of the embedded population are more likely to have heavy disks, including sources I_45 and

L_46. We thus view the observed K -band excess fraction of $\sim 9 - 15\%$ of the unobscured population to be only an approximation of the true value for the full CG 12 population.

Attributing K -band excess to an inner dusty disk, we find that the inner disk fraction of the CG 12 sample is intermediate between the youngest and older known sparse young stellar populations. For instance, the *XMM-Newton* Extended Survey of Taurus clouds included 65 classical and 50 weak-lined T-Tauri stars, of which 55 and 49, respectively, were detected in X-rays (Guedel et al. 2006; Telleschi et al. 2006). The Taurus cloud X-ray sample thus has an inner disk fraction around 50%, with most stars in the age range 0 – 2 Myr. In contrast, the 8 – 9 Myr old η Cha cluster, which is kinematically associated with the Sco-Cen Association and no longer has any molecular gas, has $\lesssim 3$ out of 15 ($\lesssim 20\%$) low-mass members with K -band excesses (Lyo et al. 2003; Luhman & Steeghs 2004), although a much higher fraction is seen at mid-infrared wavelengths (Bouwman et al. 2006). At ages around 17 – 23 Myr in the rich LCC and UCL subgroups of Sco-Cen, the disk fraction among X-ray stars is only $\sim 1\%$, although these disks may have been subject to OB star photoevaporation (Mamajek et al. 2002).

The $\sim 9 - 15\%$ inner disk fraction for CG 12 stars is in accord with our estimation that the sample has a wide range of stellar ages with a median value around 4 Myr (§7.2). The disk fraction is lower than that in Taurus and higher than that in LCC/UCL Sco-Cen, and roughly similar to that in η Cha.

5.3. Kinematics

Proper motion data are available for 23 CG 12 X-ray sources (Table 4) and can, in principle, be important for confirming membership in the cloud population and studying its dynamical evolution. CG 12 would have an unusual space motion, for example, if it were related to Galactic high-velocity clouds (e.g. Odenwald et al. 1992). Best known proper motions from catalogs compiled in NOMAD are given in Table 4. Twenty three X-ray sources have known proper motions, but some values are quite uncertain. The vector point diagram in Figure 9a plots the 17 *Chandra* stars with proper motions known within ± 10 mas yr $^{-1}$ precision. They are compared with > 3000 control sources taken from the NOMAD catalog within the *Chandra* fields. Most of the optically bright *Chandra* stars have proper motions in the field star concentration around $(\mu_{\alpha*}, \mu_{\delta}) \simeq (-10, -5)$ mas yr $^{-1}$. However, a few appear to be outliers, such as I_57 and III_8 around (-30,-30).

In Figure 9b, we compare one component of the observed proper motions to a simulated sample of nearby ($d \leq 1$ kpc) field stars using the Besançon stellar population model (see

§4). This shows that the distribution of *Chandra* stellar proper motions is typical of those of field stars in the direction of CG 12 located at distances of $0.4 \lesssim d \lesssim 1$ kpc. Thus, the proper motions of X-ray selected young stars in CG 12 can be attributed entirely to the established motions in the Galactic disk with no evidence for peculiar space motions.

6. Distance to CG 12

The distance to CG 12 is controversial, with estimates ranging from 100 to 600 pc (Maheswar et al. 2004). The closer estimates arise from assumptions of a small scale-height for the local interstellar medium (van Till et al. 1975; Keto & Myers 1986). Bourke et al. (1995b) assigned a distance of 400 pc assuming an association with the Vela-Gum region. From the optical photometry of intermediate-mass stars in the cloud, Williams et al. (1977) and Marraco & Forte (1978) obtained distance estimates around 600 pc which are commonly used by other researchers. Maheswar et al. (2004) obtained ONIR photometry of a hundred stars around the globule to derive a distance to CG 12 of 550 pc assuming they are main sequence field stars. Here we consider the distance range $300 < d < 630$ pc and use X-ray properties of the PMS members to constrain the distance further.

The proposed here method of distance determination is based on two interlocking features: PMS X-ray luminosities depend on stellar mass; and X-ray luminosities and masses scale differently with assumed distance. While it is well-established that most PMS X-rays seen in the *Chandra* band arise from violent magnetic reconnection flares above the stellar surface (Feigelson et al. 2007), it is not fully understood why it scales with stellar mass. It is quite possible that the observed $L_x - M$ correlation arises indirectly from two physical effects: a link between mass and stellar radius, and a link between X-ray emission and stellar volume or surface area (Preibisch et al. 2005; Telleschi et al. 2006). In any case, the $L_x - M$ correlation has been seen in a wide variety of PMS populations independent of the detailed age distribution, star-formation mode, cluster richness.

Some care is needed in the definition of the $L_x - M$ relation: estimates of the X-ray luminosities and masses, and the treatment of scatter in the $L_x - M$ diagram differ in various studies. In our past *Chandra* studies, we defined the $L_x - M$ relationship using the quantity $L_{t,c}$, the absorption-corrected luminosity in the “total” 0.5 – 8 keV band (see Getman et al. 2005 and notes in Table 3 below). The lightly obscured Orion COUP sample gives the regression lines $L_{t,c} = 1.44 \log M + 30.37$ and $L_{t,c} = 1.13 \log M + 30.34 \text{ erg s}^{-1}$ for masses estimated from optical spectroscopy and theoretical evolutionary tracks of Siess et al. (2000) and Palla & Stahler (1999), respectively (Preibisch et al. 2005). Getman et al. (2006) obtained $L_{t,c} = 1.99 \log M + 30.43 \text{ erg s}^{-1}$ for the Cepheus OB3b and Orion stars using

NIR photometry and Siess et al. tracks. The *XMM – Newton* XEST survey, using X-ray luminosity defined in the broader 0.3 – 10 keV band, and a bisector line rather than an ordinary least-squares regression line, gives $L_{XMM} = 1.91 \log M + 30.44 \text{ erg s}^{-1}$ using combined stellar spectroscopic results of many studies and Siess et al. tracks (Telleschi et al. 2006). We adopt here the Orion-Cepheus OB3b regression line from Getman et al. (2006), which uses stellar mass estimate methods more comparable to that of the current work, although recognizing that all the regression lines cited above lie very close to each other.

To estimate the distance to CG 12, we restrict our consideration to a highly reliable subsample of X-ray bright, completely unobscured ($MedE < 1.2 \text{ keV}$ and $\log N_H \lesssim 20 \text{ cm}^{-2}$) X-ray sources with $L_{t,c}$ values given in Table 3 and accurate photometry in Table 4. Masses are estimated from the R vs. $R - K$ color-magnitude diagram (Figure 7) using Siess et al. (2000) tracks. The sample includes twelve likely T-Tauri stars without K-band excesses of which ten are from the primary *Chandra* field (I_9, 10, 17, 23, 55, 61, 64, 69, 79, and 90), and two are from the secondary fields (II_12 and IV_3)⁷. Errors on the estimated photometric masses for the stars in the sample are derived from Monte-Carlo simulations based on the observed photometric uncertainties convolved with the Siess et al. evolutionary tracks. Errors on $L_{t,c}$ are estimated through Monte-Carlo simulations described in §4.3 of Getman et al. (2006).

Figure 10 shows the resulting X-ray luminosities and photometric masses of these stars calculated for a range of possible distances to the cloud. It is clear from the figure that the assumed distances $\lesssim 500 \text{ pc}$ (cyan, green, red symbols) are insufficient to place CG 12 PMS objects on the Orion $L_x - M$ regression line (black and grey solid lines). Distances of 550 – 630 pc (blue and violet symbols) are clearly preferable. The lower distance of 550 pc is further preferred if the recent revision to the Orion Nebula distance by Jeffries (2007) is correct⁸. Throughout our study, we adopt the distance to CG 12 of 550 pc.

We thus independently confirm that the distance to CG 12 is $> 500 \text{ pc}$ and more likely is close to 550 pc, in close agreement with the measurement by Maheswar et al. (2004) based on photometry and reddening of foreground and background field stars. An important consequence is the confirmation that the cloud is indeed located at a height of $\gtrsim 200 \text{ pc}$ above the Galactic plane. The existence of any star forming dark cloud at such Galactic location is unusual, and the cometary structure of CG 12 in such an isolated environment is even more

⁷Two more X-ray unobscured stars from the secondary fields, III_4 and III_8, are not included here due to problems with their estimated ages (see §7.2).

⁸An analysis based on the rotational properties of low-mass PMS ONC stars with exclusion of likely accreting systems suggests a distance of $390 \pm 30 \text{ pc}$, substantially closer than the commonly used $440 \pm 30 \text{ pc}$.

mysterious (§8).

7. The CG 12 stellar population

7.1. Stellar census

Five intermediate-mass stars (three B and two A stars), and several FG stars had been identified as likely members of the CG 12 region in previous ONIR studies (Williams et al. 1977). The three B stars in the region are detected by *Chandra*. The $V \sim 11$ mag B4 and $V \sim 10$ mag B7 components of the double star Herschel 4636, which illuminates the reflection nebula NGC 5367 (= GN 13.54.7 Williams et al. 1977), correspond to *Chandra* sources L_58 ($\log L_{t,c} \simeq 29.7 \text{ erg s}^{-1}$) and L_57 ($\log L_{t,c} \simeq 30.1 \text{ erg s}^{-1}$), respectively. The $V \sim 10$ mag B8 star CD -39°8583 associated with the reflection nebula GN 13.54.9 is L_74 ($\log L_{t,c} \simeq 30.2 \text{ erg s}^{-1}$). The two A stars⁹ have emission fainter than $\log L_{t,c} \lesssim 29.0 \text{ erg s}^{-1}$, the sensitivity level in our primary *Chandra* field.

These X-ray properties of the CG 12 intermediate-mass stars are consistent with past studies on A and B star samples. These stars lack both convection zones which drive surface magnetic flares and the strong radiation-driven stellar winds which drive high-temperature shocks. It is suspected that their intrinsic X-ray emission is low or absent, and some appear in *Chandra* images only when accompanied by a lower mass T-Tauri companion (e.g. Stelzer et al. 2006).

The important new *Chandra* result is the identification of nearly 60 low-mass young stars, increasing the known population of the cloud by nearly a factor of 10 (§3 and 4). Three of these are very likely embedded protostars (§7.3), while the rest are lightly-moderately obscured T-Tauri stars. As outlined in §1, the existence of these stars is expected from an extrapolation of a standard Initial Mass Function from the previously known intermediate-mass members. The five known BA stars demand the presence of ~ 80 T-Tauri stars within the mass range of $0.2 - 2 M_{\odot}$ assuming the Galactic field IMF of Kroupa (2002).

With the sensitivity limits of our X-ray observations around $\log L_{t,c} \simeq 29.0(30.0) \text{ erg s}^{-1}$ in the primary (secondary) fields, we expect our samples to be sensitive down to ~ 0.2 (0.5) M_{\odot} , and complete at masses higher than these. This inference emerges from the established statistical correlation between X-ray luminosity and stellar mass (Preibisch et al.

⁹These are sources ## 6 and 8 from Williams et al. (1977), typed as A4 and A2 by Maheswar et al. (2004). Source #8 may be powering the reflection nebula B77 146 (Bernes 1977), located just northwest of the cloud (Figure 4b).

2005; Telleschi et al. 2006). Thus, our X-ray detected sample constitutes most, but not all, of the expected low mass population.

We can estimate the star formation efficiency (SFE) of CG 12, defined as the ratio of integrated stellar mass to the total mass of molecular gas and stars. The 80 stars in the range $0.2 < M < 2 M_{\odot}$ have a total mass around $30 - 35 M_{\odot}$, and the intermediate-mass stars have a total mass around $20 M_{\odot}$, given a stellar mass around $50 M_{\odot}$. The mass of the observed molecular gas is estimated to be $100 - 250 M_{\odot}$ (§1). The implied SFE is then in the range 15%-35%. This should be considered an upper bound on the SFE since the original cloud was probably more massive prior to ablation into a cometary morphology. These values are typical among other star forming regions (Elmegreen et al. 2000, and references therein). However, it is significantly higher than the SFE we found for the much smaller and younger cometary globule IC 1396N (typical among hundred of known BRCs) where the SFE is estimated to be less than 4% based on the *Chandra* sample (Getman et al. 2007). This suggests that the triggering mechanisms in CG 12 may differ from smaller globules on the edges of HII regions.

7.2. Ages of the Unobscured Population

Stellar ages for the unobscured low-mass ($\lesssim 2 M_{\odot}$) X-ray population of CG 12 can be estimated from the color-magnitude diagram in Figure 7. These stars have $MedE \lesssim 1.2$ keV and $R \gtrsim 12$ mag located above the ZAMS. Three stars are excluded from consideration and require more study: I_29 due to inconsistency between its X-ray and NIR obscuration (§5), and III_4 and III_8 because their inferred ages are characteristic of Class 0/I protostars rather than visible T-Tauri stars (although they have normal colors in the JHK_s color-color diagram, Figure 8). Thus, 21 stars are considered in this analysis: I_9, 10, 17, 23, 35, 36, 47, 48, 50, 55, 61, 64, 68, 69, 72, 79, 80, 90, 92 from the primary field, and II_8 and II_10 from the secondary fields.

The derived photometric ages for these stars using Siess et al. (2000) PMS models in R vs. $R - K$ (which are similar to R vs. $R - H$) are shown in Figure 11 along with their formal errors, ΔAge . The errors were derived similarly to the mass errors in §6 using Monte Carlo simulations of photometric magnitudes and colors according to each source’s reported photometric errors, and placing simulated stars on PMS isochrones. The errors do not account for a possible presence of unresolved binaries or variability (Preibisch & Zinnecker 1999; Burningham et al. 2005). Unresolved binaries would tend to make objects appear up to a factor of 2 brighter, leading to an underestimation of the true age. PMS stars are known to be variable due to rotational modulation of starspots and, for classical T-

Tauri stars, due to variations in accretion. Typical starspot fluctuations are $\Delta R \simeq \Delta K \simeq 0.1$ mag (Carpenter et al. 2001; Herbst et al. 2002) and accretion variations can exceed 1 mag (Stassun et al. 2006). None of the 21 low-mass stars used in this analysis possess noticeable K_s excesses (Figure 8), so fluctuations likely do not exceed 0.1 mag. But variability often moves the star parallel to isochrones and may not contribute significantly to apparent age spreads (Burningham et al. 2005). If we add this additional uncertainty to photometric magnitudes and colors of CG 12 sources, the inferred age uncertainties increase by factors of $\sim 2-3$. We denote the derived ages as “photometric isochronal ages” in order to distinguish them from the true stellar ages. Our upcoming spectroscopic study should provide more reliable estimates of individual CG 12 stellar ages.

The distribution of the photometric isochronal ages in Figure 11, combined with the presence of several embedded protostars not plotted here (§7.3), indicates a large age spread from < 1 to ~ 20 Myr. The age spread appears real and cannot be attributed to photometric errors. There may be two or more distinct populations in CG 12: a very young embedded population forming in the molecular cores right now (§7.3) as a part or independent of a younger and richer population of T-Tauri stars with ages 1 – 10 Myr, median value around ~ 4 Myr (mean around 4.5 Myr) and a standard deviation of 2.7 Myr; and a sparse older population of likely 15 – 30 Myr stars. The latter sub-sample (I_: 36, 68, 92, and 90) also has JHK_s photometric colors close to the 50 Myr (older) isochrone in Figure 8. However, the results are also consistent with a continuous star formation history.

We note that age spreads from 0 to 30 Myr have been reported in a number of young stellar populations. Most relevant to this study, Ogura et al. (2006) find mean ages of 1 – 2.5 Myr and standard deviations of 0.6 – 2.5 Myr, with two stars around 5 Myr, in the stellar populations around four CGs. Their sample is derived from ONIR techniques that are less effective than *Chandra* images in locating older weak-lined T-Tauri stars, so the true maximum age may be older than they estimate.

Broad stellar age distributions are found in other well-studied star forming regions. Kenyon & Hartmann (1995) find a smooth age distribution from < 1 to > 10 Myr in the Taurus-Auriga clouds, although Hartmann (2003) (see also Slesnick et al. 2006) argues that the older stars are unrelated to the clouds. About 10% of the Orion Nebula Cluster membership have ages around 10 Myr with the remainder much younger around $\lesssim 1$ Myr (Slesnick et al. 2004; Palla et al. 2005, 2007). The young stellar cluster associated with σ Ori has an age spread up to ~ 30 Myr with median age of ~ 4 Myr (Oliveira et al. 2002, 2004; Sacco et al. 2006). The Chamaeleon I population shows an age range from < 1 to 10 Myr (Luhman & Steeghs 2004). In contrast, no age spread is found in the ~ 5 Myr old Upper-Sco OB association (Preibisch & Zinnecker 1999). From a theoretic-

cal perspective, researchers are actively debating whether molecular clouds are short-lived and produce brief bursts of star formation (e.g. Elmegreen et al. 2000; Hartmann et al. 2001; Ballesteros-Paredes & Hartmann 2007) or whether clouds are long-lived and produce stars in a more continuous fashion (e.g. Palla & Stahler 2000; Mouschovias et al. 2006; Krumholz & Tan 2007).

7.3. Ages of the Embedded Population

Signs of ongoing star formation in CG 12 include a bipolar molecular outflow (White 1993) and its millimeter-continuum candidate source in the CG 12S molecular core (Haikala & Olberg 2006), and the far-infrared source IRAS 13546-3941 in CG 12N, resolved in the near-infrared as a Class I visual binary protostellar system with 5'' separation (Santos et al. 1998). Here we describe the *Chandra* detection of the components of the NIR visual protostellar binary in CG 12N (I_45 and I_46), and present evidence for a newly discovered protostar in CG 12S (I_54).

Chandra sources I_45 and I_46 exhibit absorptions of $\log N_H \sim 22.1 - 22.2 \text{ cm}^{-2}$ (Table 3) which correspond to $A_V \sim 8 - 10 \text{ mag}$ assuming a standard gas-to-dust ratio from Vuong et al. (2003). This is consistent with a location near the center of the molecular core CG 12N (Figure 4b) which has a total absorption of $\sim 10 - 13 \text{ mag}$ (Haikala & Olberg 2006). Their NIR colors are consistent with Class I objects (Figure 8), although an early Class II phase is possible. Their X-ray luminosities are similar, $\log L_{t,c} \sim 30.3 - 30.5 \text{ erg s}^{-1}$, and are consistent with the brightest known solar-mass T-Tauri stars and many Class I protostars (Imanishi, Koyama, & Tsuboi 2001; Wolk et al. 2005) and are definitely the strongest among the hard X-ray sources seen through the CG 12 cloud.

Among all CG 12 *Chandra* sources with *NetCts* > 20 (Table 3), source I_54 has the hardest spectrum (*MedE* $\sim 3.2 \text{ keV}$), but it is not identified with any known ONIR source. Seen in projection against the CG 12S molecular peak (Figure 4b) where the absorption through the cloud is $\sim 6 - 8 \text{ mag}$ (Haikala & Olberg 2006), its X-ray spectrum shows a much higher absorption of $\log N_H \simeq 22.6 \text{ cm}^{-2}$ corresponding to $A_V \sim 25 \text{ mag}$. The additional absorption of $\sim 20 \text{ mag}$ that cannot be attributed to the cloud likely originates in a protostellar envelope. In IC 1396N, Getman et al. (2007) show from a *Chandra/Spitzer* comparison that such heavy absorption arises only in local protostellar envelopes, and in the Serpens cloud Giardino et al. (2007) find absorptions for all Class I protostars to be $\log N_H > 22.3 \text{ cm}^{-2}$. I_54 has an X-ray luminosity similar to the other two Class I protostars in CG 12, $\log L_{t,c} \simeq 30.3 - 30.7 \text{ erg s}^{-1}$, higher than most of the unobscured T-Tauri stars. A similar trend is seen in IC 1396N and Serpens. Finally, I_54 is one of only two

sources (along with the unobscured intermediate-mass star I_70) that show significant X-ray variability (Table 2). This is likely due to a magnetic reconnection flare during our short *Chandra* exposure. This feature excludes the possibility that I_54 might be an extragalactic contaminant; extragalactic sources, even active galactic nuclei, of this brightness do not exhibit variability over an 8 hour exposure (e.g. Bauer et al. 2003; Paolillo et al. 2004). Source I_54 thus shows all of the X-ray characteristics of a Class I protostar: hard spectrum, high absorption, high luminosity, and magnetic flaring.

We thus confirm that the CG 12 molecular globule harbors the population of very young objects with ages of $\lesssim 0.1$ Myr, typical of Class I protostars.

7.4. Spatial structure

The *Chandra* results show that the young stars are much more widely distributed than today’s cloud (Figure 4a). Previously noted cloud members, and our concentrated group of obscured X-ray stars, lie within the CG 12 cloud in a $< 1 \times 1$ pc² region. But the unobscured young X-ray emitting population is distributed widely over the four *Chandra* fields which subtend 5×5 pc² (Figure 4a). The concentration of X-ray sources inside the inner portion of the *ROSAT* detector (Figure 2), which subtends a much greater area than *Chandra*’s detector, shows that most of the X-ray population lies within the *Chandra* fields.

8. Discussion

8.1. Implications for CG star formation models

In §7.2 and 7.3, we establish that the CG 12 globule produced young stars over a period of $\gtrsim 10$ Myr, most of which likely formed around 4.5 ± 2.7 Myr ago. Many of these stars are now widely distributed around the cloud. The cloud also harbors three very young embedded protostars forming today in its molecular cores.

These findings are similar to age distributions found in other low-mass star forming regions such as Taurus-Auriga (Kenyon & Hartmann 1995) and Chamaeleon I (Luhman & Steeghs 2004) where stellar ages range over < 1 Myr to $\gtrsim 10$ Myr. These broad age ranges are inconsistent with rapid star formation scenarios where gravitational collapse occurs in one or two turbulent crossing times (Elmegreen et al. 2000; Hartmann et al. 2001; Ballesteros-Paredes & Hartmann 2007). For a cloud like CG 12 with size $1 - 2$ pc (although prior to ablation it may have been larger), the characteristic large-scale turbulent velocity will be ~ 2 km s⁻¹ (Larson

1981) with corresponding crossing time ~ 2 Myr. These rapid star formation models thus predict that all cloud members should have ages $\lesssim 2$ Myr. Instead, the CG 12 age distribution suggests either a more continuous star formation process (Palla & Stahler 2000; Mouschovias et al. 2006; Krumholz & Tan 2007; Nakamura & Li 2007), or possibly several episodes of a rapid star formation. The age distribution in CG 12 is consistent with an exponentially accelerating star formation rate (Palla & Stahler 2000) providing the characteristic timescale is several million years.

The broad age spread is also inconsistent with the rapid timescale (few $\times 10^5$ yr) predicted by simple triggered star formation models of CGs outlined in §1. However, more complex models of shock triggered star formation might explain the age distribution of CG 12 stars. Two possibilities can be considered. First, RDI simulations producing only brief durations of star formation (Lefloch & Lazareff 1994; Miao et al. 2006) modelled only small globules with initial sizes < 1 pc typical for known bright rimmed clouds (Sugitani et al. 1991) with volumes much smaller than the initial size of the atypically large CG 12 cloud. The RDI shock front may thus take millions of years to propagate through the whole CG 12 cloud during which distributed molecular cores could be compressed, triggering localized star formation at different times. Second, unlike triggering by the continuous flux of photoevaporating ultraviolet light from OB stars in HII regions, the triggering of CG 12 could arise from a sequence of distinct episodes separated by millions of years. These triggers could be the shocks of distinct supernova from a massive OB association. Astronomical evidence for these scenarios is discussed in §8.2.

The wide spatial distribution of young stars, roughly 5×5 pc² around a cloud with current size 1×2 pc², has additional implications for the star formation process. It suggests either that the cloud was originally much larger before it was ablated into a cometary morphology, or that the stars drifted from the core, or both. The members of the unobscured population of CG 12 are uniformly distributed across the field and do not show any spatial gradient in their derived photometric stellar ages that could be indicative of sequential star formation produced by a single triggering mechanism such as a propagating shock. A spatio-temporal gradient of this type has recently been seen in several other CGs and bright-rimmed clouds (Matsuyanagi et al. 2006; Getman et al. 2007; Ogura et al. 2006). Star drifting, on the other hand, requires a stellar velocity dispersion around 1 km s^{-1} which can reasonably arise either from dynamical interactions during star formation (Bate et al. 2003) or from turbulent motions in the natal gas (Feigelson 1996).

The absence of an obvious age gradient in CG 12 is not yet definitive, as our optical spectroscopy and mid-infrared *Spitzer* observations have not been completed. The addition of a spatial distribution of infrared-bright low mass stars with massive disks, as found from

Spitzer IRAC maps of IC 1396N by Getman et al. (2007), may give a crucial new clue and could establish the validity of the expected cloud ablation and sequential triggered star formation mechanism.

8.2. New observational keys to the origin of CG 12

With a strange location and orientation, and no reported external hot OB star further from the plane illuminating and ablating the globule, the origin of CG 12 is very uncertain. The best attempted explanation was made 30 years ago by Williams et al. (1977) who suggested that a large expanding high-latitude interstellar shell could have traversed CG 12 7-19 Myr ago. This shell is now called GC 323+34-021 in the Leiden-Dwingeloo H I survey (Ehlerová & Palouš 2005)¹⁰ and GIRL G318+32 in the IRAS loop catalog (Könyves et al. 2007). Produced by one or more supernova explosions from a still-unidentified association, the encounter would have drawn out the 10 pc-long tail and triggered the star formation in the globule. This explanation suffers a major difficulty: a single supernova explosion (perhaps from a runaway O star ejected from a Galactic Plane cluster) can not be responsible for such a large $\sim 20^\circ$ cavity, while a superbubble produced by many supernova remnants requires a rich high-latitude stellar cluster which has not yet been identified.

To further test this model, we searched for intermediate-mass B-type members of the hypothetical high-latitude young stellar cluster using the Henry Draper (HD) Catalogue (Cannon & Pickering 1924). Such stars should be very prominent: at $d = 550$ pc, a ZAMS B0 (B9) star without significant obscuration will have $V \simeq 5$ mag (9 mag). Figure 12a shows the spatial distribution of all known B0-B9 stars (green circles) in a $\sim 40^\circ \times 40^\circ$ area around the GIRL G318+32 IRAS loop (magenta). To discriminate stars likely physically associated with the loop region from foreground contaminants, we designate stars inside the loop having photometric distances of 350 – 700 pc derived from placement on the V vs. $V - K_s$ diagram with red + symbols in Figure 12a.

While there is no indication of a residual cluster at the center of the ~ 200 pc diameter loop, we note the presence of $\gtrsim 6$ B-type stars located only 10 – 30 pc northwest of CG 12. Stellar properties of these B-type stars, which we tentatively call the HD 120958 group, are listed in Table 5. Compared to the Orion Nebular Cluster (ONC) (Stelzer et al. 2005), the HD 120958 group has the same number of B5-B9 stars (5 late-B stars) but only one star of earlier type *vs.* 11 in the ONC where the population extends to O7. These massive stars

¹⁰Due to the limiting coverage of the Leiden-Dwingeloo H I survey, Ehlerová & Palouš (2005) report only the top part of the shell.

may be missing because they have gone supernova over the past 15 – 30 Myr, the lifetime of B1-3 stars (Hirschi et al. 2005). This sequence of supernova shocks could have elongated the CG 12 cloud into its current cometary structure and triggered repeated episodes of star formation¹¹.

The star HD 120958 deserves special attention. Among other B-type members of the group, it is the closest to CG 12 (only ~ 10 pc away providing they lie at the same distance) and is precisely positioned on the axis of the CG 12 cometary tail (Figure 12*b*). It is also the most luminous star in the region. A B5 spectral type was originally assigned in the HD catalog but later reclassified to B3Vne in the Michigan Catalogue of Houk & Fuentes-Williams (1982). Their footnotes on the star indicate Balmer line cores in emission and extremely broad lines in absorption, general observational characteristics of classical Be stars (Porter & Rivinius 2003).

While there is now a consensus that a classical Be star is a rapidly rotating B-type star that produces a disk in its equatorial plane, no certain picture of the evolutionary state of Be phenomenon is available (Porter & Rivinius 2003, and references therein). Some fraction of Be stars are produced in binaries (Gies 2000), and Be+neutron star (NS) systems represent the largest sub-class of massive X-ray binaries known (Coe 2000; Ziolkowski 2002). According to the evolutionary model of such a binary, the progenitor of the Be star acquires its rapid rotation via mass and angular momentum transfer from the primary companion, which in turn undergoes a SN stage and turns into a NS (van den Heuvel 1983). X-ray emission from Be+NS systems is usually transient.

It is thus reasonable to suggest that HD 120958, well-positioned along the geometric axis of CG 12, could be the relic of a massive binary system where the primary has evolved into a SN. The encounter of the SN remnant with the cloud could be, at least in part, responsible for both the star formation and the cometary morphology of the cloud. We have found no evidence for a transient X-ray source coincident with HD 120958¹².

Another, perhaps less plausible, scenario considering HD 120958 to be responsible for

¹¹We note that none of the known radio pulsars from the catalog of Manchester et al. (2005) shown as cyan \times symbols in Figure 12*a* lies in or near the HD 120958 group. A pulsar could be ejected from a massive binary after supernova.

¹²There is a confused history concerning a report of a transient X-ray source near the tail of CG 12 with the non-imaging Ariel V satellite (Cooke 1976). Incorrectly labelled A 0353-40 rather than A 1353-40, it does not appear in any official Ariel V source catalog including the catalog of Ariel V transients (Pye & McHardy 1983). Even if the source exists, it lies more than a degree from HD 120958 and cannot be associated with this star.

the morphology of CG 12 and origin of its stellar population, can be suggested. In this case the B3e HD 120958 star itself could be the primary ionizing source of the region. As in the hundred known cases of small bright rimmed clouds (BRCs) believed to exhibit the RDI mechanism, HD 120958 would produce an ionization front at the surface of the CG 12 cloud, which could slowly ablate and drive shocks into the cloud. In this scenario the poorly studied B77 146 nebula (Bernes 1977), located just at the surface of the cloud (Figures 1 and 4b) and interpreted as a reflection nebula powered by the A2 member of the region (Maheswar et al. 2004), could be in fact an ionization front produced by the UV radiation from HD 120958. However in comparison with other known BRCs, the CG 12 again would represent a rather atypical case with a cooler and more distant primary ionizing source. Several BRCs illuminated by a single B-type are known, but all with spectral types earlier than B2, and with distances to BRCs < 4 pc (Morgan et al. 2004; Thompson et al. 2004b).

9. Conclusions

We report results from a mosaic of four *Chandra* ACIS-I images (5×5 pc²) designed to study the young stellar population and star formation in the high-latitude cometary globule CG 12. The main findings of our study are as follows:

1. Of the 128 X-ray sources detected in the *Chandra* fields covering the globule’s head and its vicinity, 55 have been identified with known ONIR objects. In addition to several known young intermediate-mass stars, we discovered a previously unknown population of $\gtrsim 50$ T-Tauri members. Most are unobscured but some lie inside the cloud. Three proto-stars embedded in the molecular cloud cores are detected, one of which is newly reported. We establish that the remaining ~ 70 X-ray sources are likely contaminants, mostly extragalactic, based on simulations of Galactic and extragalactic populations, the presence or absence of ONIR counterparts, spatial distribution, and X-ray properties.

2. Based on available ONIR photometry of the CG 12 T-Tauri stars, we infer they are mostly low-mass $0.2 - 0.7 M_{\odot}$ stars, $\sim 9 - 15\%$ of which possess K_s disks. This low fraction of K -excess stars is similar to older T-Tauri populations (e.g. η Cha with age $8 - 9$ Myr) and substantially lower than that of younger PMS populations (e.g. the Taurus clouds).

3. Using the known $L_x - M$ corrections, we combine X-ray and ONIR properties of the unobscured T-Tauri stars to independently confirm that the distance to CG 12 must be > 500 pc, and probably in the range $550 - 630$ pc. This strengthens previous ONIR findings that CG 12 is indeed located $\gtrsim 200$ pc above the Galactic plane, and that its cometary morphology with no signs of nearby hot OB stars is unusual.

4. An evaluation of stellar ages gives a median photometric isochronal age of ~ 4 Myr with a large spread from < 1 Myr to $\sim 10 - 20$ Myr. The X-ray properties of three deeply embedded stars confirm the protostellar classification and previous infrared-radio findings of ongoing star formation in the globule’s head.

5. Assuming the Galactic field IMF for the unobscured YSO population of CG 12, we estimate a total population of ~ 80 stars associated with CG 12 with masses $> 0.2 M_{\odot}$. The star formation efficiency of the globule is in the range 15–35%, typical for active star forming regions, but above that seen in smaller molecular globules with star formation triggered by UV shock fronts.

6. The age and spatial distribution of young stars is consistent with that seen in other star forming regions, but is inconsistent with a simple model of radiative driven implosion often applied to explain CG morphology and star formation. This suggests either that CG 12 is atypically large so that a triggering shock takes millions of years to traverse the cloud, or that CG 12 has been subject to several distinct episodes of triggering and ablation over millions of years.

7. Examination of the vicinity of the cloud leads to a revised scenario for the origin of the CG 12 star forming region. We identify a group of B-type stars northwest of CG 12 and infer that a dozen expected early O-B3 type members are missing. These could be the source of multiple SN explosions triggering star formation in the cloud over an extended period of 15 – 30 Myr. The B3e star HD 120958 is the closest and most luminous member of the group, lying 10 pc (projected) from the globule head in the correct orientation to ablate the cloud into its cometary structure. It might itself be the primary ionizing source driving an RDI shock into the CG 12 cloud, or might be the relic of a massive binary system that has undergone SN explosion.

We thank Sangwook Park and Oleg Kargaltsev for useful discussions on H I shells and pulsars. This work is supported by *Chandra* guest observer grant SAO G06-7007X (PI: K.V. Getman). This work was also supported by the *Chandra* ACIS Team (G. Garmire, PI) through NASA contract NAS8-38252. This publication makes use of data products from the Two Micron All Sky Survey (a joint project of the University of Massachusetts and the Infrared Processing and Analysis Center/California Institute of Technology, funded by NASA and NSF). This research makes use of the SIMBAD database, operated at CDS, Strasbourg, France.

REFERENCES

- Anders, E., & Grevesse, N. 1989, *Geochim. Cosmochim. Acta*, 53, 197
- Argiroffi, C., Favata, F., Flaccomio, E., Maggio, A., Micela, G., Peres, G., & Sciortino, S. 2006, *A&A*, 459, 199
- Arnaud, K. A. 1996, in *Data Analysis Software and Systems V*, ed. G. H. Jacoby & J. Barnes (San Francisco:ASP), 17
- Ballesteros-Paredes, J., & Hartmann, L. 2007, *Revista Mexicana de Astronomia y Astrofisica*, 43, 123
- Baraffe, I., Chabrier, G., Allard, F., & Hauschildt, P. H. 1998, *A&A*, 337, 403
- Barger, A. J., et al. 2003, *AJ*, 126, 632
- Bate, M. R., Bonnell, I. A., & Bromm, V. 2003, *MNRAS*, 339, 577
- Bauer, F. E., et al. 2003, *Astronomische Nachrichten*, 324, 175
- Bernes, C. 1977, *A&AS*, 29, 65
- Bertoldi, F. 1989, *ApJ*, 346, 735
- Bessell, M. S., & Brett, J. M. 1988, *PASP*, 100, 1134
- Bok, B. J., & Reilly, E. F. 1947, *ApJ*, 105, 255
- Bourke, T. L., Hyland, A. R., & Robinson, G. 1995a, *MNRAS*, 276, 1052
- Bourke, T. L., Hyland, A. R., Robinson, G., James, S. D., & Wright, C. M. 1995b, *MNRAS*, 276, 1067
- Bouwman, J., Lawson, W. A., Dominik, C., Feigelson, E. D., Henning, T., Tielens, A. G. G. M., & Waters, L. B. F. M. 2006, *ApJ*, 653, L57
- Brandt, W. N., et al. 2001, *AJ*, 122, 2810
- Burningham, B., Naylor, T., Littlefair, S. P., & Jeffries, R. D. 2005, *MNRAS*, 363, 1389
- Cannon, A. J., & Pickering, E. C. 1924, *Annals of Harvard College Observatory*, 99, 1
- Carpenter, J. M., Hillenbrand, L. A., & Skrutskie, M. F. 2001, *AJ*, 121, 3160
- Cash, W. 1979, *ApJ*, 228, 939

- Clarke, C. J., Bonnell, I. A., & Hillenbrand, L. A. 2000, *Protostars and Planets IV*, 151
- Coe, M. J. 2000, *IAU Colloq. 175: The Be Phenomenon in Early-Type Stars*, 214, 656
- Cooke, B. A. 1976, *Nature*, 261, 564
- Cutri, R. M., et al. 2003, 2MASS All Sky Catalog of point sources, published by The IRSA 2MASS All-Sky Point Source Catalog, NASA/IPAC Infrared Science Archive. <http://irsa.ipac.caltech.edu/applications/Gator/>
- Deharveng, L., Zavagno, A., & Caplan, J. 2005, *A&A*, 433, 565
- De Vries, C. H., Narayanan, G., & Snell, R. L. 2002, *ApJ*, 577, 798
- Dickey, J. M., & Lockman, F. J. 1990, *ARA&A*, 28, 215
- Dutra, C. M., & Bica, E. 2002, *A&A*, 383, 631
- Ehlerová, S., & Palouš, J. 2005, *A&A*, 437, 101
- Elmegreen, B. G., Efremov, Y., Pudritz, R. E., & Zinnecker, H. 2000, *Protostars and Planets IV*, 179
- Elmegreen, B. G. 2000b, *ApJ*, 530, 277
- Feigelson, E. D. 1996, *ApJ*, 468, 306
- Feigelson, E. D., Broos, P., Gaffney, J. A., Garmire, G., Hillenbrand, L. A., Pravdo, S. H., Townsley, L., & Tsuboi, Y. 2002, *ApJ*, 574, 258
- Feigelson, E. D., Lawson, W. A., & Garmire, G. P. 2003, *ApJ*, 599, 1207
- Feigelson, E. D., et al. 2005, *ApJS*, 160, 379
- Feigelson, E., Townsley, L., Güdel, M., & Stassun, K. 2007, *Protostars and Planets V*, 313
- Garmire, G. P., Bautz, M. W., Ford, P. G., Nousek, J. A., & Ricker, G. R. 2003, *Proc. SPIE*, 4851, 28
- Gehrels, N. 1986, *ApJ*, 303, 336
- Getman, K. V., Feigelson, E. D., Townsley, L., Bally, J., Lada, C. J., & Reipurth, B. 2002, *ApJ*, 575, 354
- Getman, K. V., Flaccomio, E., Broos, P. et al. 2005a, *ApJS*, 160, 319

- Getman, K. V., Feigelson, E. D., Grosso, N., McCaughrean, M. J., Micela, G., Broos, P., Garmire, G., & Townsley, L. 2005b, *ApJS*, 160, 353
- Getman, K. V., Feigelson, E. D., Townsley, L., Broos, P., Garmire, G., & Tsujimoto, M. 2006, *ApJS*, 163, 306
- Getman, K. V., Feigelson, E. D., Garmire, G., Broos, P., & Wang, J. 2007, *ApJ*, 654, 316
- Giardino, G., Favata, F., Micela, G., Sciortino, S., & Winston, E. 2007, *A&A*, 463, 275
- Gies, D. R. 2000, *IAU Colloq. 175: The Be Phenomenon in Early-Type Stars*, 214, 668
- Gorti, U., & Hollenbach, D. 2002, *ApJ*, 573, 215
- Guedel, M., et al. 2006, *A&A*, in press (astro-ph/0609160)
- Haikala, L. K., & Olberg, M. 2006, *A&A*, in press (astro-ph/0609820)
- Haisch, K. E., Jr., Lada, E. A., & Lada, C. J. 2001, *ApJ*, 553, L153
- Hartmann, L., Ballesteros-Paredes, J., & Bergin, E. A. 2001, *ApJ*, 562, 852
- Hartmann, L. 2003, *ApJ*, 585, 398
- Hawarden, T. G., & Brand, P. W. J. L. 1976, *MNRAS*, 175, 19P
- Heiles, C. 1984, *ApJS*, 55, 585
- Herbst, W., Bailer-Jones, C. A. L., Mundt, R., Meisenheimer, K., & Wackermann, R. 2002, *A&A*, 396, 513
- Herschel, J. F. W. S. 1847, London, Smith, Elder and co., 1847
- Hirschi, R., Meynet, G., & Maeder, A. 2005, *A&A*, 433, 1013
- Houk, N., & Fuentes-Williams, T. H. 1982, *BAAS*, 14, 615
- Hünsch, M., Schmitt, J. H. M. M., Sterzik, M. F., & Voges, W. 1999, *A&AS*, 135, 319
- Imanishi, K., Koyama, K., & Tsuboi, Y. 2001, *ApJ*, 557, 747
- Jeffries, R. D. 2007, *MNRAS*, 159
- Johnson, H. L. 1966, *ARA&A*, 4, 193
- Kessel-Deynet, O., & Burkert, A. 2003, *MNRAS*, 338, 545

- Keto, E. R., & Myers, P. C. 1986, *ApJ*, 304, 466
- Könyves, V., Kiss, C., Moór, A., Kiss, Z. T., & Tóth, L. V. 2007, *A&A*, 463, 1227
- Krumholz, M. R., & Tan, J. C. 2007, *ApJ*, 654, 304
- Larson, R. B. 1981, *MNRAS*, 194, 809
- Lawson, W. A., Crause, L. A., Mamajek, E. E., & Feigelson, E. D. 2001, *MNRAS*, 321, 57
- Lefloch, B., & Lazareff, B. 1994, *A&A*, 289, 559
- Lefloch, B., & Lazareff, B. 1995, *A&A*, 301, 522
- Lehmann, I., et al. 2001, *A&A*, 371, 833
- Luhman, K. L., & Rieke, G. H. 1998, *ApJ*, 497, 354
- Luhman, K. L., & Steeghs, D. 2004, *ApJ*, 609, 917
- Lyo, A.-R., Lawson, W. A., Mamajek, E. E., Feigelson, E. D., Sung, E.-C., & Crause, L. A. 2003, *MNRAS*, 338, 616
- Lyons, L. 1991, *A Practical Guide to Data Analysis for Physical Science Students* (Cambridge: Cambridge Univ. Press)
- Kenyon, S. J., & Hartmann, L. 1995, *ApJS*, 101, 117
- Kroupa, P. 2002, *Science*, 295, 82
- Magakian, T. Yu. 2003, *A&A*, 399, 141
- Maheswar, G., Manoj, P., & Bhatt, H. C. 2004, *MNRAS*, 355, 1272
- Mamajek, E. E., Lawson, W. A., & Feigelson, E. D. 2000, *ApJ*, 544, 356
- Mamajek, E. E., Meyer, M. R., & Liebert, J. 2002, *AJ*, 124, 1670
- Manchester, R. N., Hobbs, G. B., Teoh, A., & Hobbs, M. 2005, *AJ*, 129, 1993
- Marraco, H. G., & Forte, J. C. 1978, *ApJ*, 224, 473
- Matsuyanagi, I., Itoh, Y., Sugitani, K., Oasa, Y., Mukai, T., & Tamura, M. 2006, *PASJ*, 58, L29
- Megeath, S. T., Hartmann, L., Luhman, K. L., & Fazio, G. G. 2005, *ApJ*, 634, L113

- Meyer, M. R., Calvet, N., & Hillenbrand, L. A. 1997, *AJ*, 114, 288
- Miao, J., White, G. J., Nelson, R., Thompson, M., & Morgan, L. 2006, *MNRAS*, 369, 143
- Monet, D. G., et al. 2003, *AJ*, 125, 984
- Moretti, A., Campana, S., Lazzati, D., & Tagliaferri, G. 2003, *ApJ*, 588, 696
- Morgan, L. K., Thompson, M. A., Urquhart, J. S., White, G. J., & Miao, J. 2004, *A&A*, 426, 535
- Morrison, R. & McCammon, D. 1983, *ApJ*, 270, 119
- Mouschovias, T. C., Tassis, K., & Kunz, M. W. 2006, *ApJ*, 646, 1043
- Nakamura, F., & Li, Z.-Y. 2007, *ArXiv Astrophysics e-prints*, astro-ph/0703152
- Neckel, T., & Vehrenberg, H. 1990, Duesseldorf: Treugesell-Verlag, 1990
- Odenwald, S., Fischer, J., Lockman, F. J., & Stemwedel, S. 1992, *ApJ*, 397, 174
- Oey, M. S., & García-Segura, G. 2004, *ApJ*, 613, 302
- Ogura, K., Sugitani, K., & Pickles, A. 2002, *AJ*, 123, 2597
- Ogura, K., Chauhan, N., Pandey, A. K., Bhatt, B. C., Ojha, D., & Itoh, Y. 2006, *PASJ*, in press, astro-ph/0611845
- Oliveira, J. M., Jeffries, R. D., Kenyon, M. J., Thompson, S. A., & Naylor, T. 2002, *A&A*, 382, L22
- Oliveira, J. M., Jeffries, R. D., & van Loon, J. T. 2004, *MNRAS*, 347, 1327
- Palla, F., & Stahler, S. W. 1999, *ApJ*, 525, 772
- Palla, F., & Stahler, S. W. 2000, *ApJ*, 540, 255
- Palla, F., & Stahler, S. W. 2002, *ApJ*, 581, 1194
- Palla, F., Randich, S., Flaccomio, E., & Pallavicini, R. 2005, *ApJ*, 626, L49
- Palla, F., Randich, S., Pavlenko, Y. V., Flaccomio, E., & Pallavicini, R. 2007, *ApJ*, 659, L41
- Paolillo, M., Schreier, E. J., Giacconi, R., Koekemoer, A. M., & Grogin, N. A. 2004, *ApJ*, 611, 93

- Porter, J. M., & Rivinius, T. 2003, *PASP*, 115, 1153
- Preibisch, T., & Zinnecker, H. 1999, *AJ*, 117, 2381
- Preibisch, T., & Feigelson, E. D. 2005a, *ApJS*, 160, 390
- Preibisch, T., et al. 2005b, *ApJS*, 160, 401
- Pye, J. P., & McHardy, I. M. 1983, *MNRAS*, 205, 875
- Reipurth, B. 1983, *A&A*, 117, 183
- Robin, A. C., Reyl e, C., Derri ere, S., & Picaud, S. 2003, *A&A*, 409, 523
- Sacco, G. G., Randich, S., Franciosini, E., Pallavicini, R., & Palla, F. 2006, *A&A*, in press (astro-ph/0611880)
- Santos, N. C., Yun, J. L., Santos, C. A., & Marreiros, R. G. 1998, *AJ*, 116, 1376
- Schmitt, J. H. M. M., Fleming, T. A., & Giampapa, M. S. 1995, *ApJ*, 450, 392
- Schmitt, J. H. M. M. 1997, *A&A*, 318, 215
- Siess, L., Dufour, E., & Forestini, M. 2000, *A&A*, 358, 593
- Slesnick, C. L., Hillenbrand, L. A., & Carpenter, J. M. 2004, *ApJ*, 610, 1045
- Slesnick, C. L., Carpenter, J. M., Hillenbrand, L. A., & Mamajek, E. E. 2006, *AJ*, 132, 2665
- Smith, R. K., Brickhouse, N. S., Liedahl, D. A., & Raymond, J. C. 2001, *ApJ*, 556, L91
- Stassun, K. G., van den Berg, M., Feigelson, E., & Flaccomio, E. 2006, *ApJ*, 649, 914
- Steffen, A. T., Barger, A. J., Capak, P., Cowie, L. L., Mushotzky, R. F., & Yang, Y. 2004, *AJ*, 128, 1483
- Stelzer, B., Flaccomio, E., Montmerle, T., Micela, G., Sciortino, S., Favata, F., Preibisch, T., & Feigelson, E. D. 2005, *ApJS*, 160, 557
- Stelzer, B., Hu elamo, N., Micela, G., & Hubrig, S. 2006, *A&A*, 452, 1001
- Sugitani, K., Fukui, Y., & Ogura, K. 1991, *ApJS*, 77, 59
- Sugitani, K., & Ogura, K. 1994, *ApJS*, 92, 163
- Sugitani, K., Tamura, M., & Ogura, K. 1995, *ApJ*, 455, L39

- Telleschi, A., Guedel, M., Briggs, K. R., Audard, M., & Palla, F. 2006, *A&A*, in press (astro-ph/0612338)
- Thompson, M. A., White, G. J., Morgan, L. K., Miao, J., Fridlund, C. V. M., & Huldgtgren-White, M. 2004, *A&A*, 414, 1017
- Thompson, M. A., Urquhart, J. S., & White, G. J. 2004b, *A&A*, 415, 627
- Townsley, L. K., Broos, P. S., Nousek, J. A., & Garmire, G. P. 2002, *Nuclear Instruments and Methods in Physics Research A*, 486, 751
- Townsley, L. K., Feigelson, E. D., Montmerle, T., Broos, P. S., Chu, Y.-H., & Garmire, G. P. 2003, *ApJ*, 593, 874
- Townsley, L. K., Broos, P. S., Feigelson, E. D., Garmire, G. P., & Getman, K. V. 2006, *AJ*, 131, 2164
- Urquhart, J. S., Thompson, M. A., Morgan, L. K., & White, G. J. 2006, *A&A*, 450, 625
- van den Heuvel, E. P. J. 1983, *Accretion-Driven Stellar X-ray Sources*, 303
- van Till, H., Loren, R., & Davis, J. 1975, *ApJ*, 198, 235
- Vuong, M. H., Montmerle, T., Grosso, N., Feigelson, E. D., Verstraete, L., & Ozawa, H. 2003, *A&A*, 408, 581
- Webb, R. A., Zuckerman, B., Platais, I., Patience, J., White, R. J., Schwartz, M. J., & McCarthy, C. 1999, *ApJ*, 512, L63
- Weisskopf, M. C., Brinkman, B., Canizares, C., Garmire, G., Murray, S., & Van Speybroeck, L. P. 2002, *PASP*, 114, 1
- White, G. J. 1993, *A&A*, 274, L33
- Williams, P. M., Brand, P. W. J. L., Longmore, A. J., & Hawarden, T. G. 1977, *MNRAS*, 180, 709
- Wolk, S. J., Harnden, F. R., Jr., Flaccomio, E., Micela, G., Favata, F., Shang, H., & Feigelson, E. D. 2005, *ApJS*, 160, 423
- Yonekura, Y., Hayakawa, T., Mizuno, N., Mine, Y., Mizuno, A., Ogawa, H., & Fukui, Y. 1999, *PASJ*, 51, 837
- Zacharias, N., Monet, D. G., Levine, S. E., Urban, S. E., Gaume, R., & Wycoff, G. L. 2004a, *Bulletin of the American Astronomical Society*, 36, 1418

Zacharias, N., Urban, S. E., Zacharias, M. I., Wycoff, G. L., Hall, D. M., Monet, D. G., & Rafferty, T. J. 2004b, *AJ*, 127, 3043

Ziolkowski, J. 2002, *Memorie della Societa Astronomica Italiana*, 73, 1038

Table 1. CG 12 Observations

Field	ObsID	Start Time	Exposure (ks)	R.A. (J2000.0) (hh:mm:ss.ss)	Decl. (J2000.0) (dd:mm:ss.ss)	Roll Angle (deg)
I	6423	2006 Apr 15 16:19:17	30.8	13:57:44.52	-39:58:48.31	11.5
II	6424	2006 Jun 02 07:25:09	3.1	13:57:42.87	-39:43:01.76	285.0
III	6425	2006 Apr 13 08:44:08	3.1	13:56:19.40	-39:42:47.94	14.7
IV	6426	2006 Apr 15 12:54:20	3.1	13:56:19.40	-39:58:48.09	11.1

Note. — ObsID values are from the *Chandra* Observation Catalog. Start Times are in UT. Exposure times are the sum of Good Time Intervals (GTIs) for the CCD at the telescope aim point (CCD3) minus 1.3% to account for CCD readouts. The aimpoints and roll angles are obtained from the satellite aspect solution before astrometric correction was applied.

Table 2. Basic Source Properties

Source			Position				Extracted Counts					Characteristics				
Field	Seq	CXOU J	α_{J2000}	δ_{J2000}	Err	θ	Net	Δ Net	Bkgd	Net	PSF	Signif	Anom ^a	Var ^b	EFFExp	Med E
(1)	(2)	(3)	(deg)	(deg)	('')	(')	Full	Full	Full	Hard	Frac	(13)	(14)	(15)	(ks)	(keV)
			(4)	(5)	(6)	(7)	(8)	(9)	(10)	(11)	(12)	(13)	(14)	(15)	(16)	(17)
I	1	135657.01–395349.7	209.237580	-39.897144	1.25	10.38	8.2	5.0	10.8	6.3	0.91	1.5	a	20.1	2.23
I	2	135702.10–395409.6	209.258790	-39.902694	0.67	9.37	34.4	6.9	6.6	21.9	0.89	4.6	a	21.2	2.61
I	3	135703.91–395455.0	209.266310	-39.915279	1.01	8.70	8.4	4.3	5.6	7.5	0.90	1.7	a	22.5	3.73
I	4	135704.65–400123.2	209.269380	-40.023117	1.24	8.06	4.5	3.4	3.5	2.5	0.90	1.1	g...	...	22.2	3.45
I	5	135706.07–395822.2	209.275330	-39.972848	0.35	7.38	64.2	8.7	2.8	22.3	0.90	7.0	a	24.6	1.61
I	6	135708.01–395821.9	209.283380	-39.972767	0.65	7.01	13.1	4.5	2.9	8.1	0.90	2.6	a	25.0	3.04
I	7	135709.47–400142.7	209.289470	-40.028538	0.44	7.32	39.4	7.0	2.6	9.4	0.89	5.2	a	22.7	1.47
I	8	135709.55–400528.4	209.289810	-40.091237	1.21	9.45	6.5	4.2	6.5	1.9	0.89	1.4	a	20.6	3.79
I	9	135711.34–400234.7	209.297260	-40.042982	0.20	7.39	201.1	14.8	2.9	11.1	0.90	13.1	a	24.1	1.10
I	10	135712.03–400050.2	209.300140	-40.013965	0.36	6.55	41.8	7.1	1.2	5.2	0.90	5.5	g...	...	14.2	1.16
I	11	135712.31–400026.5	209.301316	-40.007375	0.46	6.39	22.3	5.4	1.7	7.9	0.90	3.7	a	22.8	1.55
I	12	135713.12–400754.7	209.304700	-40.131877	1.09	10.91	15.4	5.9	12.6	4.6	0.90	2.4	a	21.0	1.77
I	13	135716.11–400000.8	209.317150	-40.000243	0.69	5.58	5.6	3.2	1.4	4.1	0.90	1.5	a	27.0	3.13
I	14	135716.75–395234.2	209.319800	-39.876190	0.47	8.20	50.6	8.0	5.4	13.1	0.91	5.9	a	22.9	1.50
I	15	135716.93–400049.7	209.320560	-40.013822	0.70	5.66	5.8	3.2	1.2	4.2	0.90	1.5	a	25.7	3.74
I	16	135717.03–395657.1	209.320970	-39.949204	0.45	5.59	13.0	4.3	1.0	10.3	0.91	2.7	a	26.5	3.67
I	17	135717.06–395710.5	209.321110	-39.952928	0.33	5.51	25.1	5.6	0.9	0.4	0.91	4.1	g...	...	23.6	1.00
I	18	135717.70–400057.7	209.323780	-40.016043	0.40	5.57	18.8	5.0	1.2	9.3	0.90	3.4	b	24.7	1.85
I	19	135719.53–395543.6	209.331375	-39.928782	0.31	5.70	30.0	6.1	1.0	11.3	0.91	4.5	g...	...	22.7	1.70
I	20	135719.80–395426.2	209.332527	-39.907288	0.72	6.45	7.4	3.5	1.6	1.9	0.90	1.8	a	25.1	1.70
I	21	135721.59–395255.1	209.339986	-39.881984	0.52	7.35	25.3	5.8	2.7	9.3	0.89	4.0	a	23.9	1.79
I	22	135722.99–400609.8	209.345811	-40.102729	0.89	8.44	9.6	4.4	5.4	2.7	0.90	1.9	g...	...	20.5	1.73
I	23	135723.21–395749.6	209.346750	-39.963795	0.16	4.20	44.5	7.2	0.5	4.6	0.90	5.7	a	28.1	1.03
I	24	135724.23–400112.3	209.350960	-40.020094	0.12	4.57	109.4	11.0	0.6	72.5	0.90	9.5	a	25.8	2.69
I	25	135724.84–395512.0	209.353501	-39.920011	0.48	5.22	8.8	3.7	1.2	6.1	0.91	2.1	a	26.6	2.31
I	26	135725.67–395608.0	209.356960	-39.935574	0.19	4.50	38.5	6.8	0.5	12.6	0.89	5.3	b	27.4	1.57
I	27	135725.84–395837.2	209.357680	-39.977017	0.26	3.59	12.6	4.1	0.4	0.7	0.89	2.7	a	28.8	0.99
I	28	135725.96–395303.0	209.358180	-39.884182	0.52	6.77	18.6	5.1	2.4	14.3	0.89	3.3	a	23.0	3.86
I	29	135726.01–395627.0	209.358409	-39.940860	0.26	4.26	17.5	4.8	0.5	2.6	0.90	3.3	a	27.8	1.22
I	30	135726.93–400459.3	209.362228	-40.083166	0.66	7.04	11.7	4.3	2.3	6.5	0.90	2.4	g...	...	22.6	2.04
I	31	135727.30–395714.8	209.363763	-39.954133	0.38	3.65	5.7	3.0	0.3	5.8	0.90	1.6	a	28.5	5.16
I	32	135727.52–400032.1	209.364700	-40.008920	0.36	3.69	6.7	3.2	0.3	4.8	0.89	1.8	g...	...	25.6	3.32
I	33	135727.84–395602.5	209.366020	-39.934051	0.19	4.23	31.5	6.2	0.5	22.7	0.89	4.7	a	27.5	2.56
I	34	135728.00–400845.9	209.366700	-40.146102	2.20	10.45	6.6	3.7	3.4	3.6	0.90	1.5	ge..	...	5.3	3.27
I	35	135728.46–400500.6	209.368622	-40.083516	0.68	6.93	9.9	4.0	2.1	0.8	0.89	2.2	a	24.2	0.93
I	36	135732.16–395836.4	209.384027	-39.976781	0.27	2.38	5.8	3.0	0.2	0.9	0.89	1.6	a	29.8	1.03
I	37	135733.02–395752.6	209.387610	-39.964632	0.09	2.39	49.8	7.6	0.2	18.9	0.89	6.1	b	29.5	1.63
I	38	135734.10–400300.4	209.392116	-40.050133	0.55	4.65	4.5	2.8	0.5	2.7	0.89	1.3	a	28.6	3.60
I	39	135734.99–395130.0	209.395832	-39.858361	0.91	7.53	8.4	4.0	3.6	3.5	0.89	1.8	a	21.3	1.91
I	40	135735.90–395518.4	209.399585	-39.921800	0.30	3.87	11.6	4.0	0.4	8.7	0.90	2.5	g...	...	24.2	2.91
I	41	135737.47–395559.8	209.406151	-39.933285	0.37	3.12	4.7	2.8	0.3	1.8	0.90	1.4	a	28.6	1.70
I	42	135738.25–395948.1	209.409381	-39.996701	0.17	1.56	10.9	3.8	0.1	3.9	0.89	2.5	g...	...	15.7	1.95
I	43	135738.39–400153.9	209.409979	-40.031663	0.22	3.31	13.7	4.3	0.3	6.8	0.89	2.8	a	28.6	1.95
I	44	135738.44–400347.6	209.410170	-40.063249	0.29	5.12	24.9	5.6	1.1	2.2	0.90	4.0	b	28.1	1.28
I	45	135738.92–395558.4	209.412181	-39.932889	0.10	3.03	64.7	8.6	0.3	33.8	0.90	7.1	a	28.7	2.07
I	46	135738.96–395601.2	209.412345	-39.933668	0.08	2.98	88.7	9.9	0.3	57.8	0.90	8.5	a	28.7	2.65
I	47	135739.74–395403.7	209.415615	-39.901054	0.36	4.83	15.4	4.5	0.6	4.6	0.90	3.0	g...	...	18.0	1.20
I	48	135740.17–400325.0	209.417393	-40.056956	0.27	4.69	22.3	5.3	0.7	4.5	0.91	3.8	a	25.8	1.03

Table 2—Continued

Source			Position				Extracted Counts					Characteristics				
Field	Seq #	CXOU J	α_{J2000} (deg)	δ_{J2000} (deg)	Err ($''$)	θ ($'$)	Net Full	Δ Net Full	Bkgd Full	Net Hard	PSF Frac	Signif	Anom ^a	Var ^b	EffExp (ks)	Med E (keV)
(1)	(2)	(3)	(4)	(5)	(6)	(7)	(8)	(9)	(10)	(11)	(12)	(13)	(14)	(15)	(16)	(17)
I	49	135740.72–400130.6	209.419693	-40.025179	0.27	2.80	6.8	3.2	0.2	6.8	0.89	1.8	...	a	30.2	2.97
I	50	135741.23–400137.5	209.421810	-40.027086	0.20	2.89	13.8	4.3	0.2	2.8	0.89	2.8	...	a	29.6	1.20
I	51	135741.35–400502.5	209.422313	-40.084031	0.57	6.27	11.5	4.1	1.5	3.9	0.90	2.4	...	a	27.1	1.45
I	52	135741.76–400239.0	209.424040	-40.044179	0.44	3.88	4.6	2.8	0.4	4.7	0.89	1.4	...	a	29.4	4.75
I	53	135741.91–400605.0	209.424660	-40.101402	0.85	7.30	7.3	3.7	2.7	5.1	0.89	1.7	...	a	24.6	2.17
I	54	135742.28–395846.7	209.426185	-39.979655	0.06	0.43	80.8	9.5	0.2	70.9	0.90	8.1	...	c	30.5	3.18
I	55	135742.89–400227.4	209.428717	-40.040969	0.11	3.67	78.7	9.4	0.3	5.7	0.90	7.9	...	a	29.0	1.16
I	56	135743.83–395404.6	209.432660	-39.901288	0.44	4.73	9.3	3.7	0.7	3.5	0.89	2.2	...	a	25.5	1.55
I	57	135743.94–395847.1	209.433110	-39.979759	0.06	0.12	73.8	9.1	0.2	16.9	0.90	7.7	...	a	30.6	1.32
I	58	135744.13–395844.1	209.433880	-39.978938	0.12	0.10	19.9	5.0	0.1	8.9	0.90	3.6	...	a	30.5	1.91
I	59	135744.48–400445.9	209.435360	-40.079443	0.61	5.96	8.4	3.7	1.6	4.9	0.90	2.0	...	a	27.5	2.17
I	60	135744.98–400154.3	209.437430	-40.031771	0.28	3.10	7.8	3.4	0.2	5.8	0.90	2.0	g...	...	26.4	2.30
I	61	135745.11–400107.0	209.438000	-40.018635	0.07	2.32	80.8	9.5	0.2	10.9	0.89	8.0	...	a	28.5	1.06
I	62	135747.13–400631.7	209.446390	-40.108819	0.63	7.74	20.3	5.4	3.7	8.4	0.89	3.4	...	a	25.4	1.47
I	63	135748.43–395650.0	209.451804	-39.947247	0.22	2.11	7.8	3.4	0.2	6.9	0.89	2.0	...	a	29.7	2.80
I	64	135749.94–395512.7	209.458085	-39.920220	0.20	3.74	23.5	5.4	0.5	3.7	0.89	3.9	...	a	28.4	1.18
I	65	135752.62–400238.1	209.469270	-40.043940	0.46	4.13	5.5	3.0	0.5	5.6	0.90	1.5	...	a	26.9	3.85
I	66	135753.12–395546.7	209.471341	-39.929653	0.05	3.44	329.6	18.7	0.4	136.7	0.89	17.2	...	a	28.8	1.70
I	67	135753.16–400148.5	209.471519	-40.030144	0.30	3.43	8.7	3.5	0.3	6.8	0.89	2.1	...	a	29.4	3.31
I	68	135753.75–395730.9	209.473997	-39.958600	0.15	2.19	16.9	4.6	0.1	1.9	0.89	3.2	...	a	27.1	1.03
I	69	135754.33–395522.0	209.476393	-39.922805	0.10	3.92	103.5	10.7	0.5	3.7	0.90	9.2	...	a	26.3	1.09
I	70	135754.49–400430.3	209.477060	-40.075099	0.08	6.01	606.7	25.2	2.3	141.5	0.91	23.6	...	c	27.1	1.41
I	71	135754.52–395735.7	209.477187	-39.959917	0.22	2.26	8.8	3.5	0.2	6.9	0.90	2.1	...	a	28.2	3.07
I	72	135755.70–395923.2	209.482109	-39.989788	0.16	2.22	15.8	4.5	0.2	0.9	0.89	3.1	...	a	29.7	1.13
I	73	135755.86–395354.0	209.482760	-39.898356	0.46	5.36	10.7	4.0	1.3	1.2	0.91	2.3	...	a	26.6	1.09
I	74	135756.05–400418.7	209.483570	-40.071875	0.14	5.93	199.8	14.7	2.2	15.5	0.90	13.1	...	a	27.2	1.16
I	75	135757.00–395210.5	209.487505	-39.869595	0.37	7.05	43.1	7.3	2.9	12.1	0.90	5.5	...	a	23.4	1.61
I	76	135757.23–400434.0	209.488500	-40.076120	0.60	6.25	10.9	4.1	2.1	1.6	0.90	2.3	...	a	26.8	1.66
I	77	135757.86–400034.5	209.491124	-40.009595	0.21	3.11	13.7	4.3	0.3	7.8	0.89	2.8	...	a	29.2	2.07
I	78	135758.38–395313.5	209.493257	-39.887103	0.47	6.18	16.1	4.8	1.9	5.8	0.90	3.0	...	a	24.1	1.66
I	79	135758.41–395921.8	209.493380	-39.989391	0.09	2.71	73.8	9.1	0.2	6.9	0.89	7.7	g...	...	23.8	1.07
I	80	135800.02–395551.3	209.500088	-39.930935	0.28	4.18	14.4	4.4	0.6	1.6	0.89	2.9	...	a	28.1	0.96
I	81	135803.45–395750.4	209.514410	-39.964014	0.15	3.75	42.5	7.1	0.5	0.0	0.90	5.6	...	a	28.9	0.82
I	82	135805.13–400316.4	209.521400	-40.054557	0.44	5.96	16.4	4.8	1.6	6.9	0.90	3.1	...	a	25.1	1.86
I	83	135805.27–395928.2	209.521963	-39.991168	0.19	4.03	32.6	6.3	0.4	9.7	0.90	4.8	g...	...	24.8	1.55
I	84	135805.93–395357.6	209.524710	-39.899349	0.43	6.35	22.0	5.4	2.0	0.8	0.91	3.7	g...	...	18.1	1.01
I	85	135806.86–400336.6	209.528601	-40.060190	0.37	6.43	31.0	6.3	2.0	10.6	0.90	4.6	...	a	26.5	1.77
I	86	135808.18–395949.8	209.534120	-39.997189	0.22	4.64	33.3	6.3	0.7	14.5	0.89	4.8	...	a	27.7	1.76
I	87	135808.79–395335.5	209.536630	-39.893215	0.31	6.98	60.9	8.5	2.1	32.6	0.89	6.8	g...	...	16.2	2.01
I	88	135809.96–395243.9	209.541530	-39.878883	0.68	7.79	15.4	4.9	3.6	8.0	0.89	2.8	...	a	22.3	2.08
I	89	135814.01–400338.1	209.558390	-40.060602	0.77	7.43	9.7	4.1	3.3	8.8	0.90	2.1	...	b	25.1	3.83
I	90	135818.24–395640.5	209.576018	-39.944607	0.49	6.80	24.1	5.6	1.9	2.7	0.89	3.9	...	a	23.6	1.12
I	91	135819.05–395743.6	209.579406	-39.962114	0.88	6.70	6.3	3.4	1.7	5.9	0.89	1.6	...	a	23.8	3.55
I	92	135825.59–395819.0	209.606638	-39.971947	0.95	7.88	8.6	4.0	3.4	0.8	0.89	1.9	g...	...	21.1	0.90
I	93	135828.51–395703.9	209.618817	-39.951088	1.59	8.60	4.6	3.7	5.4	4.5	0.90	1.1	ge...	...	15.3	5.76
II	1	135650.79–393750.1	209.211628	-39.630588	2.00	11.29	9.7	3.8	1.3	4.1	0.90	2.2	...	a	2.1	1.61
II	2	135705.32–394644.0	209.272175	-39.778915	1.14	8.11	8.5	3.5	0.5	0.6	0.90	2.0	...	b	2.4	1.80
II	3	135723.05–393733.5	209.346059	-39.625979	0.82	6.67	7.8	3.4	0.2	2.8	0.89	2.0	...	a	2.5	1.74

Table 2—Continued

Source			Position				Extracted Counts					Characteristics				
Field	Seq #	CXOU J	α_{J2000} (deg)	δ_{J2000} (deg)	Err ($''$)	θ ($'$)	Net Full	Δ Net Full	Bkgd Full	Net Hard	PSF Frac	Signif	Anom ^a	Var ^b	EffExp (ks)	Med E (keV)
(1)	(2)	(3)	(4)	(5)	(6)	(7)	(8)	(9)	(10)	(11)	(12)	(13)	(14)	(15)	(16)	(17)
II	4	135724.13–395112.6	209.350578	-39.853513	1.48	8.94	6.4	3.2	0.6	0.6	0.90	1.7	a	2.3	1.09
II	5	135724.90–393550.3	209.353780	-39.597320	0.98	7.98	11.6	4.0	0.4	0.0	0.90	2.5	a	2.2	1.07
II	6	135733.00–394652.4	209.387539	-39.781243	0.50	4.29	4.9	2.8	0.1	2.0	0.89	1.5	b	2.7	1.73
II	7	135740.45–393543.1	209.418564	-39.595325	0.51	7.32	30.7	6.1	0.3	7.8	0.90	4.6	g...	...	2.4	1.25
II	8	135747.35–394730.1	209.447304	-39.791695	0.48	4.55	7.9	3.4	0.1	0.0	0.91	2.0	a	2.7	1.04
II	9	135753.08–394332.1	209.471201	-39.725588	0.19	2.03	11.0	3.8	0.0	3.0	0.89	2.5	a	3.0	1.22
II	10	135800.20–395003.8	209.500835	-39.834416	0.85	7.78	13.6	4.3	0.4	1.8	0.90	2.8	b	2.3	1.10
II	11	135802.32–395002.4	209.509678	-39.834026	1.47	7.95	4.6	2.8	0.4	4.8	0.90	1.3	a	2.4	4.11
II	12	135808.06–394319.4	209.533621	-39.722060	0.30	4.85	20.9	5.1	0.1	5.0	0.89	3.7	b	2.6	1.09
II	13	135809.81–393544.4	209.540881	-39.595672	1.63	8.94	5.5	3.0	0.5	3.6	0.90	1.5	a	2.2	4.66
II	14	135817.30–394226.0	209.572109	-39.707235	1.10	6.65	4.7	2.8	0.3	4.8	0.90	1.4	a	2.5	3.64
III	1	135545.24–394715.6	208.938512	-39.787686	1.06	7.94	8.5	3.5	0.5	3.8	0.89	2.1	a	2.4	1.50
III	2	135609.27–394516.7	209.038653	-39.754653	0.35	3.15	5.0	2.8	0.0	3.0	0.89	1.5	a	3.0	2.26
III	3	135612.23–394503.3	209.050995	-39.750940	0.28	2.64	6.0	3.0	0.0	1.0	0.90	1.7	a	3.0	1.19
III	4	135617.60–393918.2	209.073348	-39.655064	0.09	3.51	102.0	10.6	0.0	7.0	0.89	9.2	a	2.9	1.04
III	5	135628.82–393944.9	209.120117	-39.662490	0.25	3.55	13.0	4.1	0.0	7.0	0.89	2.8	a	2.9	2.12
III	6	135629.78–394000.5	209.124093	-39.666816	0.31	3.43	8.0	3.4	0.0	2.0	0.89	2.0	a	2.9	1.51
III	7	135645.86–394551.7	209.191100	-39.764368	0.62	5.94	8.9	3.5	0.1	2.9	0.90	2.2	a	2.4	1.48
III	8	135647.84–394456.0	209.199342	-39.748896	0.27	5.87	46.9	7.4	0.1	0.9	0.90	5.9	b	2.7	1.01
III	9	135653.62–394307.8	209.223442	-39.718845	0.77	6.59	8.8	3.5	0.2	4.9	0.89	2.1	a	2.6	2.68
IV	1	135542.11–400258.4	208.925468	-40.049574	1.23	8.27	7.5	3.4	0.5	3.7	0.89	1.9	a	2.3	1.99
IV	2	135543.16–395930.6	208.929866	-39.991841	0.84	6.98	9.7	3.7	0.3	1.9	0.91	2.3	a	2.5	1.06
IV	3	135544.12–395818.1	208.933845	-39.971716	0.32	6.78	55.8	8.0	0.2	3.9	0.90	6.5	a	2.5	1.03
IV	4	135600.77–400040.8	209.003224	-40.011360	0.41	4.03	7.0	3.2	0.0	0.0	0.90	1.8	a	2.6	0.85
IV	5	135608.75–395440.9	209.036497	-39.911368	0.34	4.60	14.9	4.4	0.1	3.9	0.91	3.0	b	2.7	1.38
IV	6	135628.52–400022.6	209.118870	-40.006280	0.22	2.35	9.0	3.5	0.0	2.0	0.89	2.2	a	3.0	1.45
IV	7	135632.73–395830.6	209.136378	-39.975186	0.32	2.57	5.0	2.8	0.0	2.0	0.89	1.5	a	2.9	1.51
IV	8	135635.51–395647.6	209.147971	-39.946560	0.30	3.68	10.0	3.7	0.0	5.0	0.89	2.3	a	2.7	1.48
IV	9	135637.93–395810.7	209.158048	-39.969665	0.43	3.60	5.0	2.8	0.0	0.0	0.89	1.5	a	2.9	1.15
IV	10	135640.74–400710.2	209.169789	-40.119524	2.27	9.31	6.4	3.2	0.6	1.5	0.90	1.7	ge..	...	1.4	1.77
IV	11	135644.43–400004.1	209.185160	-40.001161	0.31	4.96	21.9	5.2	0.1	11.0	0.91	3.8	a	2.7	1.83
IV	12	135705.14–400351.4	209.271443	-40.064305	1.76	10.11	7.1	3.4	0.9	4.5	0.90	1.8	a	2.2	2.64

Note. — Column 1: *Chandra* ACIS-I fields surveyed in the CG 12 region (I - primary pointing; II, III, and IV - secondary pointings). Column 2: X-ray source number. Column 3: IAU designation. Columns 4-5: Right ascension and declination for epoch J2000.0 in degrees. Column 6: Positional uncertainty. Column 7: Off-axis angle. Columns 8-9: Estimated net counts from extracted area in total energy band (0.5 – 8.0) keV and their 1σ errors. Column 10: Estimated background counts from extracted area in total energy band. Column 11: Estimated net counts from extracted area in hard energy band (2 – 8) keV. Column 12: Fraction of the PSF at the fiducial energy of 1.497 keV enclosed within the extracted area. Note that a reduced PSF fraction (significantly below 90%) may indicate that the source is in a crowded region or on the edge of the field. Column 13: Source significance in sigma. Column 14: Source anomalies described by a set of flags, see the text note^a below for details. Column 15: Variability characterization based on K-S statistics, see the text note^b below for details. Column 16: Source effective exposure in ks. Column 17: The background-corrected median photon energy in the total 0.5 – 8 keV energy band.

^aSource anomalies: g = fractional time that source was on a detector (FRACEXPO from *mkarf*) is < 0.9 ; e = source on field edge; p = source piled up; s = source on readout streak.

^bSource variability: a = no evidence for variability; b = possibly variable; c = definitely variable. No test is performed for sources with fewer than 4 total full-band counts. No value is reported for sources in chip gaps or on field edges.

Table 3. X-ray Spectroscopy for Photometrically Selected Sources: Thermal Plasma Fits

		Source			Spectral Fit ^a		X-ray Luminosities ^b			
Field	Seq	CXOU J	Net	Med E	$\log N_H$	kT	$\log L_h$	$\log L_{h,c}$	$\log L_t$	$\log L_{t,c}$
(1)	(2)	(3)	(counts)	(keV)	(cm^{-2})	(keV)	(8)	(9)	(10)	(11)
	#							(ergs s^{-1})		
I	2	135702.10–395409.6	34.4	2.61	–1.0 21.7 +0.5	–11.7 13.0	29.71	29.73	29.80	29.90
I	5	135706.07–395822.2	64.2	1.61	20.0	11.7	29.82	29.82	29.99	29.99
I	7	135709.47–400142.7	39.4	1.47	21.5	2.5	29.49	29.51	29.72	29.88
I	9	135711.34–400234.7	201.1	1.10	20.0	1.2	29.49	29.49	30.26	30.26
I	10	135712.03–400050.2	41.8	1.16	20.0	1.2	29.08	29.08	29.82	29.83
I	11	135712.31–400026.5	22.3	1.55	21.6 +0.3	–1.4 2.6	29.25	29.27	29.45	29.63
I	14	135716.75–395234.2	50.6	1.50	21.6	4.1	29.76	29.78	29.91	30.05
I	17	135717.06–395710.5	25.1	1.00	20.0	0.8	28.21	28.21	29.36	29.37
I	19	135719.53–395543.6	30.0	1.70	–0.9 21.7 +0.5	3.9	29.62	29.64	29.76	29.92
I	21	135721.59–395255.1	25.3	1.79	21.0	15.0	29.43	29.43	29.56	29.57
I	23	135723.21–395749.6	44.5	1.03	20.0	1.1	28.65	28.65	29.53	29.53
I	24	135724.23–400112.3	109.4	2.69	–0.2 22.2 +0.2	–4.0 6.8	30.35	30.42	30.40	30.62
I	26	135725.67–395608.0	38.5	1.57	21.8	1.37	29.17	29.22	29.54	29.92
I	33	135727.84–395602.5	31.5	2.56	21.9	15.0	29.81	29.83	29.86	29.97
I	37	135733.02–395752.6	49.8	1.63	21.2 +0.5	–3.0 5.5	29.65	29.66	29.82	29.89
I	44	135738.44–400347.6	24.9	1.28	21.3	1.5	28.92	28.94	29.35	29.51
I	45	135738.92–395558.4	64.7	2.07	22.1	–1.6 3.2 +4.6	29.93	29.99	30.02	30.29
I	46	135738.96–395601.2	88.7	2.65	–0.3 22.2 +0.2	–3.0 5.4	30.23	30.30	30.27	30.53
I	48	135740.17–400325.0	22.3	1.03	21.1	0.5	27.60	27.61	29.17	29.37
I	54	135742.28–395846.7	80.8	3.18	–0.2 22.6 +0.2	–1.6 3.6 +8.3	30.28	30.45	30.30	30.74
I	55	135742.89–400227.4	78.7	1.16	20.3	1.3	29.09	29.09	29.79	29.81
I	57	135743.94–395847.1	73.8	1.32	–0.4 21.6 +0.3	–0.5 1.5 +0.5	29.43	29.47	29.80	30.07
I	58	135744.13–395844.1	19.9	1.91	21.9	3.1	29.30	29.35	29.43	29.66
I	61	135745.11–400107.0	80.8	1.06	20.0	1.5	29.22	29.22	29.83	29.83
I	62	135747.13–400631.7	20.3	1.47	–1.2 21.8 +0.3	1.5	28.92	28.97	29.22	29.54
I	64	135749.94–395512.7	23.5	1.18	20.0	2.0	28.91	28.91	29.36	29.36
I	66	135753.12–395546.7	329.6	1.70	–0.2 21.4 +0.2	–2.4 6.5 +6.4	30.55	30.57	30.69	30.77
I	69	135754.33–395522.0	103.5	1.09	20.0	1.3	29.24	29.24	29.94	29.95
I	70	135754.49–400430.3	606.7	1.41	–0.3 21.2 +0.2	–0.2 2.1 +0.5	30.48	30.49	30.80	30.91
I	74	135756.05–400418.7	199.8	1.16	20.0	1.6	29.68	29.68	30.25	30.25
I	75	135757.00–395210.5	43.1	1.61	–0.8 21.6 +0.3	–1.9 3.2	29.60	29.62	29.78	29.93
I	79	135758.41–395921.8	73.8	1.07	20.0	1.2	29.15	29.15	29.89	29.89

Table 3—Continued

		Source			Spectral Fit ^a		X-ray Luminosities ^b			
Field	Seq	CXOU J	Net	Med E	$\log N_H$	kT	$\log L_h$	$\log L_{h,c}$	$\log L_t$	$\log L_{t,c}$
(1)	(2)	(3)	(counts)	(keV)	(cm^{-2})	(keV)	(8)	(9)	(10)	(11)
	#							(ergs s^{-1})		
I	81	135803.45–395750.4	42.5	0.82	20.0	0.4	27.67	27.67	29.58	29.58
I	83	135805.27–395928.2	32.6	1.55	–0.7 22.1 +0.2	–0.4 1.1 +1.6	29.31	29.43	29.57	30.25
I	84	135805.93–395357.6	22.0	1.01	20.0	1.1	28.61	28.61	29.45	29.45
I	85	135806.86–400336.6	31.0	1.77	–0.4 22.0 +0.5	–1.6 2.2 +4.0	29.47	29.53	29.62	29.94
I	86	135808.18–395949.8	33.3	1.76	21.6 +0.5	–2.7 4.0	29.53	29.56	29.68	29.82
I	87	135808.79–395335.5	60.9	2.01	–0.3 22.2 +0.2	–1.1 2.3 +2.8	30.16	30.26	30.25	30.64
I	90	135818.24–395640.5	24.1	1.12	20.0	1.7	28.85	28.85	29.38	29.38
II	7	135740.45–393543.1	30.7	1.25	21.0 +0.6	–1.0 2.5 +6.7	30.30	30.31	30.61	30.68
II	12	135808.06–394319.4	21.0	1.09	20.0	1.3	29.61	29.61	30.28	30.28
III	4	135617.60–393918.2	102.0	1.04	20.0	1.1	30.06	30.06	30.88	30.88
III	8	135647.84–394456.0	46.9	1.01	20.0	1.0	29.59	29.59	30.58	30.58
IV	3	135544.12–395818.1	55.8	1.03	20.0	0.9	29.67	29.67	30.69	30.69
IV	11	135644.43–400004.1	21.9	1.83	21.4	15.0	30.51	30.52	30.60	30.66

Note. — Columns 1-5: For convenience, these columns reproduce the source identification, photometric net counts, and median energy data from Table 2. Columns 6-7: Best-fit values for the column density and plasma temperature parameters. See the text note^a below for details. Columns 8-11: X-ray luminosities obtained from spectral analysis. See the text note^b below for details.

^aAll fits used the “wabs(apec)” model in *XSPEC* and assumed $0.3Z_{\odot}$ abundances. Uncertainties represent 90% confidence intervals. More significant digits are used for uncertainties < 0.1 in order to avoid large rounding errors; for consistency, the same number of significant digits is used for both lower and upper uncertainties. Uncertainties are missing when *XSPEC* was unable to compute them or when their values were so large that the parameter is effectively unconstrained. Fitted values with $\log N_H < 20.0 \text{ cm}^{-2}$ are truncated at 20.0 because ACIS-I spectra are insensitive to differences in very low column densities. Fitted values with $kT > 15 \text{ keV}$ are truncated at 15 keV because the data often cannot discriminate between very high-temperature values.

^bX-ray luminosities are calculated assuming a distance of 550 pc. h = hard band (2–8 keV); t = total band (0.5–8 keV). Absorption-corrected luminosities are subscripted with a c.

Table 4—Continued

Field	Seq	CXOU J	NOMAD	Sep1	Mah04	V^a	R^b	$\mu_{\alpha*}$	μ_{δ}	2MASS	Sep2	J	H	K_s	F1
(1)	(2)	(3)	(4)	($''$) (5)	(6)	(mag) (7)	(mag) (8)	(mas/yr) (9)	(mas/yr) (10)	(11)	($''$) (12)	(mag) (13)	(mag) (14)	(mag) (15)	(16)
I	50	135741.23-400137.5	0499-0310431	0.4	18.92	13574121-4001377	0.4	14.56±0.03	13.86±0.04	13.64±0.05	AAA000
I	51	135741.35-400502.5	0499-0310433	0.9	18.57	13574135-4005027	0.2	15.12±0.05	14.65±0.07	14.23±0.09	AAA000
I	52	135741.76-400239.0
I	53	135741.91-400605.0
I	54	135742.28-395846.7
I	55	135742.89-400227.4	0499-0310438	0.0	...	17.63	15.62	-10.4±5.1	-4.2±5.4	13574288-4002273	0.2	13.11±0.02	12.48±0.03	12.27±0.02	AAA000
I	56	135743.83-395404.6	0500-0311054	0.3	13574381-3954045	0.3	14.94±0.04	13.69±0.04	13.27±0.03	AAA000
I	57	135743.94-395847.1	0500-0311055	0.2	...	10.26	9.75	-31.9±1.2	-32.1±1.7	13574395-3958471	0.0	8.87±0.01	8.07±0.09	7.26±0.06	AAAecc
I	58	135744.13-395844.1	0500-0311056	0.1	...	10.70	13574412-3958441	0.1	8.57±0.07	8.01±...	7.15±...	AUUc00
I	59	135744.48-400445.9
I	60	135744.98-400154.3
I	61	135745.11-400107.0	0499-0310446	0.1	...	15.16	15.57	-17.0±5.4	2.3±5.1	13574510-4001071	0.2	12.65±0.02	11.89±0.02	11.69±0.02	AAA000
I	62	135747.13-400631.7
I	63	135748.43-395650.0
I	64	135749.94-395512.7	0500-0311069	0.4	27-2	19.20±0.03	17.70±0.02	13574993-3955127	0.0	14.87±0.04	13.95±0.04	13.73±0.04	AAA000
I	65	135752.62-400238.1
I	66	135753.12-395546.7	0500-0311079	0.2	18.99	13575312-3955467	0.0	17.07±0.21	16.14±0.19	15.58±0.22	CCD000
I	67	135753.16-400148.5
I	68	135753.75-395730.9	0500-0311080	0.3	28-2	20.78±0.06	18.99±0.04	13575374-3957308	0.2	15.73±0.08	14.98±0.07	14.63±0.11	AAA000
I	69	135754.33-395522.0	0500-0311083	0.1	29-2	14.83±0.01	13.80±0.01	-9.8±5.2	-1.0±5.2	13575434-3955220	0.1	11.70±0.02	10.99±0.02	10.74±0.02	AAA000
I	70	135754.49-400430.3	0499-0310486	0.1	...	14.22	10.68	-18.0±5.4	-9.3±5.2	13575447-4004303	0.2	11.93±0.02	11.19±0.02	10.93±0.02	AAA000
I	71	135754.52-395735.7
I	72	135755.70-395923.2	0500-0311091	0.4	30-2	19.55±0.04	17.78±0.02	13575568-3959230	0.3	14.29±0.03	13.49±0.03	13.20±0.04	AAA000
I	73	135755.86-395354.0	0501-0308284	0.6	18.02	-22.0±6.0	-12.0±10.0	13575588-3953538	0.4	16.14±0.09	15.22±0.10	15.19±0.17	AACc00
I	74	135756.05-400418.7	0499-0310492	0.7	...	10.08	8.07	-10.2±0.9	-1.4±1.4	13575601-4004192	0.7	9.71±0.02	9.65±0.02	9.57±0.02	AAA000
I	75	135757.00-395210.5
I	76	135757.23-400434.0
I	77	135757.86-400034.5
I	78	135758.38-395313.5
I	79	135758.41-395921.8	0500-0311111	0.1	34-2	14.50±0.01	13.63±0.01	-5.4±5.2	-4.6±5.2	13575840-3959217	0.1	11.97±0.02	11.30±0.02	11.04±0.02	AAA000
I	80	135800.02-395551.3	0500-0311124	0.6	37-2	17.32±0.02	16.05±0.01	6.0±15.0	-12.0±4.0	13580000-3955516	0.3	13.39±0.02	12.64±0.02	12.36±0.02	AAA000
I	81	135803.45-395750.4	0500-0311153	0.2	...	9.12	8.55	-12.8±1.0	-11.0±1.1	13580345-3957503	0.1	7.39±0.01	6.97±0.05	6.78±0.02	AAA000
I	82	135805.13-400316.4
I	83	135805.27-395928.2
I	84	135805.93-395357.6	0501-0308376	0.5	...	16.03	12.27	13580592-3953582	0.6	14.57±0.08	13.91±0.09	13.30±0.08	AAA000
I	85	135806.86-400336.6
I	86	135808.18-395949.8
I	87	135808.79-395335.5
I	88	135809.96-395243.9	0501-0308405	1.1	19.03
I	89	135814.01-400338.1
I	90	135818.24-395640.5	0500-0311275	0.9	...	17.17	17.21	13581826-3956415	1.0	14.59±0.03	13.98±0.04	13.76±0.05	AAA000
I	91	135819.05-395743.6
I	92	135825.59-395819.0	0500-0311326	1.2	18.32	13582566-3958193	0.9	15.06±0.04	14.41±0.04	14.18±0.07	AAA000
I	93	135828.51-395703.9
II	1	135650.79-393750.1
II	2	135705.32-394644.0	0502-0308192	0.3	...	17.35	16.98	13570530-3946441	0.2	14.16±0.03	13.29±0.03	12.68±0.02	AAA000
II	3	135723.05-393733.5
II	4	135724.13-395112.6
II	5	135724.90-393550.3	0504-0309673	1.2	...	9.48	9.39	-8.0±1.0	-7.1±1.0	13572492-3935492	1.2	9.18±0.03	9.07±0.03	9.02±0.03	AAA000

Table 4—Continued

Field	Seq #	CXOU J	NOMAD	Sep1 ('')	Mah04	V^a (mag)	R^a (mag)	$\mu_{\alpha*}$ (mas/yr)	μ_{δ} (mas/yr)	2MASS	Sep2 ('')	J (mag)	H (mag)	K_s (mag)	F1
(1)	(2)	(3)	(4)	(5)	(6)	(7)	(8)	(9)	(10)	(11)	(12)	(13)	(14)	(15)	(16)
II	6	135733.00-394652.4
II	7	135740.45-393543.1	0504-0309808	0.9	18.95	14.0±21.0	-36.0±3.0
II	8	135747.35-394730.1	0502-0308546	0.7	...	14.74	14.47	-12.2±5.4	10.9±5.5	13574730-3947305	0.7	12.55±0.03	11.90±0.02	11.73±0.02	AAA000
II	9	135753.08-394332.1	0502-0308588	0.4	19.42
II	10	135800.20-395003.8	0501-0308317	0.7	...	15.08	15.21	-11.6±5.2	0.8±5.1	13580020-3950044	0.6	12.75±0.02	12.09±0.02	11.87±0.03	AAA000
II	11	135802.32-395002.4
II	12	135808.06-394319.4	0502-0308710	0.6	...	17.41	11.38	-30.4±1.5	-7.2±2.1	13580805-3943200	0.6	10.28±0.02	9.97±0.03	9.94±0.02	AAA000
II	13	135809.81-393544.4
II	14	135817.30-394226.0
III	1	135545.24-394715.6
III	2	135609.27-394516.7
III	3	135612.23-394503.3
III	4	135617.60-393918.2	0503-0304712	1.0	...	17.53	14.33	-28.0±7.0	-20.0±20.0	13561764-3939181	0.5	10.94±0.02	10.28±0.02	10.03±0.02	AAA000
III	5	135628.82-393944.9
III	6	135629.78-394000.5	0503-0304807	1.8	18.98	-60.0±11.0	-32.0±10.0	13562990-3940005	1.4	16.42±0.13	16.11±0.22	16.91±...	BDU000
III	7	135645.86-394451.7	0502-0308035	0.7	...	16.72	16.87	13564584-3944510	0.7	15.49±0.06	15.04±0.07	14.98±0.13	AAB000
III	8	135647.84-394456.0	0502-0308051	0.4	...	17.39	13.22	-31.4±5.1	-24.5±5.1	13564783-3944555	0.5	10.32±0.02	9.67±0.03	9.36±0.02	AAA000
III	9	135653.62-394307.8	0502-0308095	1.6	18.23
IV	1	135542.11-400258.4
IV	2	135543.16-395930.6	0500-0310205	0.3	18.98
IV	3	135544.12-395818.1	0500-0310215	0.4	...	12.93	12.43	-21.9±5.1	-10.2±5.1	13554414-3958184	0.4	11.06±0.02	10.59±0.03	10.47±0.02	AAA000
IV	4	135600.77-400040.8
IV	5	135608.75-395440.9
IV	6	135628.52-400022.6
IV	7	135632.73-395830.6
IV	8	135635.51-395647.6
IV	9	135637.93-395810.7
IV	10	135640.74-400710.2
IV	11	135644.43-400004.1	0499-0310040	0.6	19.03
IV	12	135705.14-400351.4	0499-0310205	1.8	18.97

Note. — Column 1: *Chandra* ACIS-I fields surveyed in the CG 12 region (I - primary pointing; II, III, and IV - secondary pointings). Column 2: X-ray source number. Column 3: IAU designation. Column 4: NOMAD identifier. Column 5: *Chandra*-NOMAD positional offset. Column 6: Source identifier from Maheswar et al. (2004) in the format: star number - region number. Columns 7-8: V and R magnitudes, see the text note^a below for details. Columns 9-10: “Best” proper motions and their mean errors from catalogs compiled in NOMAD. $\mu_{\alpha*} = \mu_{\alpha} \times \cos(\delta)$. Column 11: 2MASS name. Column 12: *Chandra*-2MASS positional offset. Columns 13-15: 2MASS JHK_s magnitudes and their formal statistical errors. Column 16: 2MASS photometry quality and confusion-contamination flag.

^aWhen formal statistical errors are given, V and R magnitudes are from Maheswar et al. (2004). V magnitudes for 3 B-type stars, I_57, I_58, and I_74, are from Williams et al. (1977). Otherwise V and R magnitudes are from NOMAD catalog, in which case all V magnitudes except for the *Chandra* source I_81 are from YB6 (= USNO unpublished) catalog, and all R magnitudes except for the *Chandra* source I_57 are from USNO-B1.0 catalog (R magnitudes from USNO-B1.0 are second red magnitudes R_2 , except for the *Chandra* sources I_70 and II_9, for which it is a first red magnitude R_1). For the *Chandra* source I_81 V magnitude is from Tycho-2 catalog, and for the *Chandra* source I_57 R magnitude is from UCAC2 catalog.

Table 5. B-type members of the stellar group northwest of CG 12

ID	R.A. (J2000.0) (hh:mm:ss.ss)	Decl. (J2000.0) (dd:mm:ss.ss)	Sp. Type	V (mag)	K_s (mag)	π (mas)
(1)	(2)	(3)	(4)	(5)	(6)	(7)
HD 120958	13:53:28.228	-39:03:25.92	B3Vne	7.61	7.613	2.20 ± 0.85
HD 120124	13:48:15.113	-38:34:12.43	B8V	9.19	9.384	...
HD 119627	13:45:00.702	-38:28:52.39	B7IV/V	8.94	9.006	...
HD 119484	13:44:13.497	-38:46:29.62	B8IV/V	9.38	9.332	...
HD 119338	13:43:25.294	-38:15:23.55	B5V	8.91	9.177	1.76 ± 1.01
HD 119277	13:43:00.718	-38:20:08.45	B9	8.81	9.053	...

Note. — Column 1: Source identification from HD catalog. Columns 2-5: Source position, spectral type, and V magnitude from SIMBAD. Column 6: K_s magnitude from 2MASS catalog. Column 7. Parallax from SIMBAD.

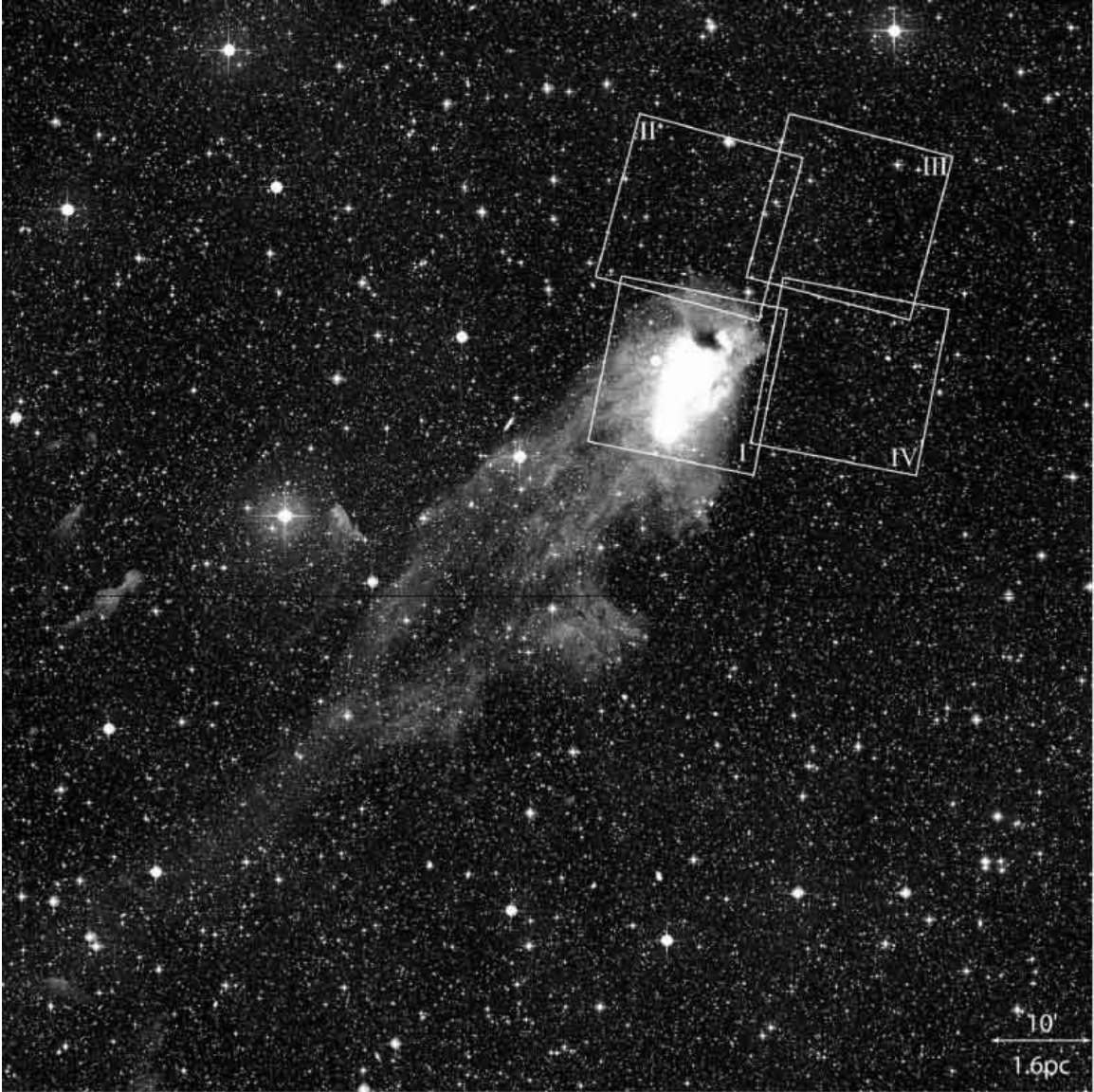


Fig. 1.— An optical image covering $\sim 1.8^\circ \times 1.8^\circ$ of the CG 12 neighborhood from the Digitized Sky Survey (DSS). The four *Chandra* ACIS-I fields, $17' \times 17'$ each, are outlined and labelled. A dark molecular cloud lies in the head of the globule, and is superposed by three nebulous reflection nebulae: NGC 5367 (=GN 13.54.7), GN 13.54.9, and B77 146.

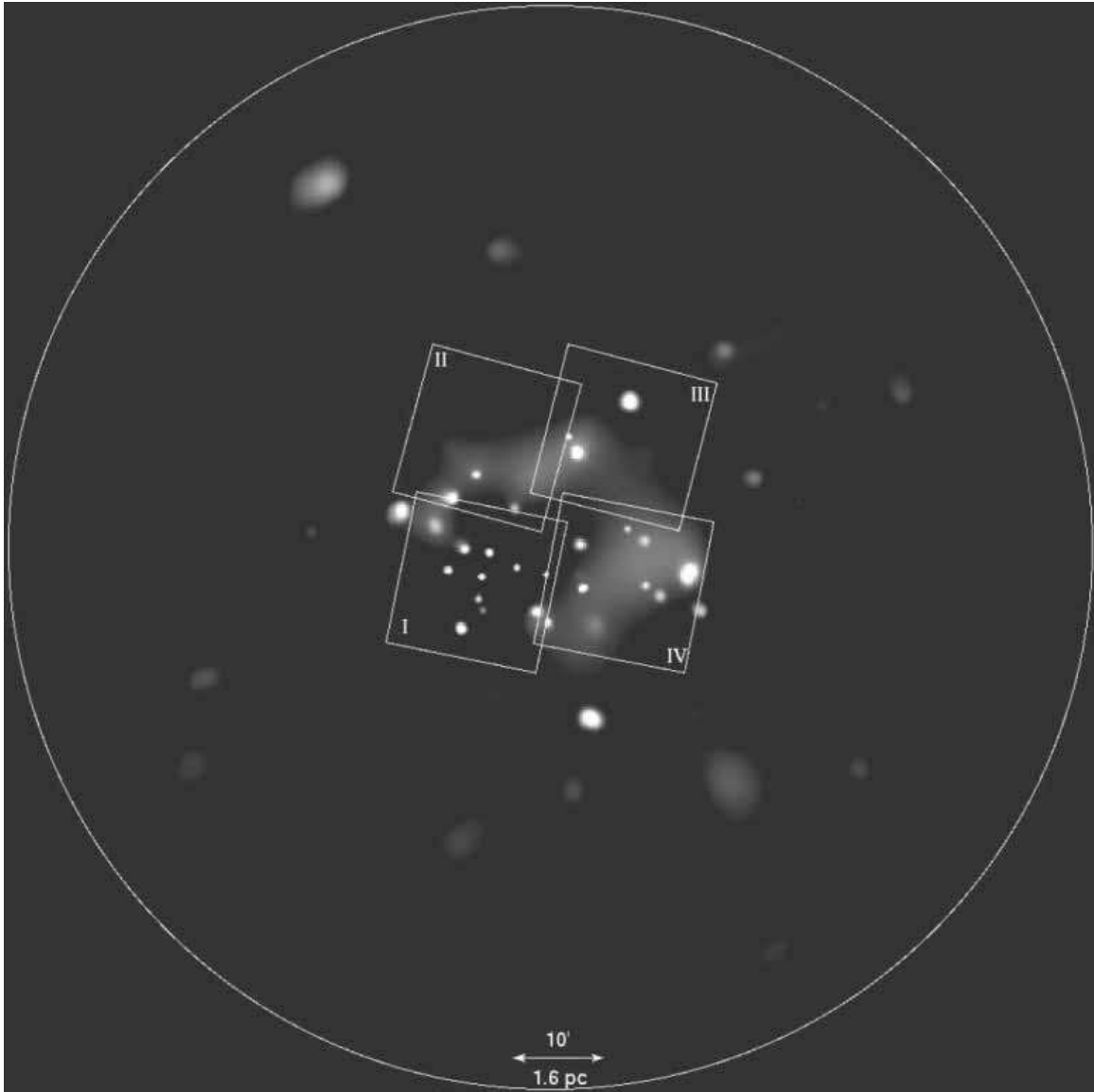


Fig. 2.— Adaptively smoothed *ROSAT*-PSPC image of the CG 12 neighborhood with logarithmic gray scales. The four ACIS-I *Chandra* fields are outlined and labelled. The $\sim 2^\circ$ in diameter *ROSAT*-PSPC field of view is outlined by the white circle. About 30 X-ray point sources are seen on the image.

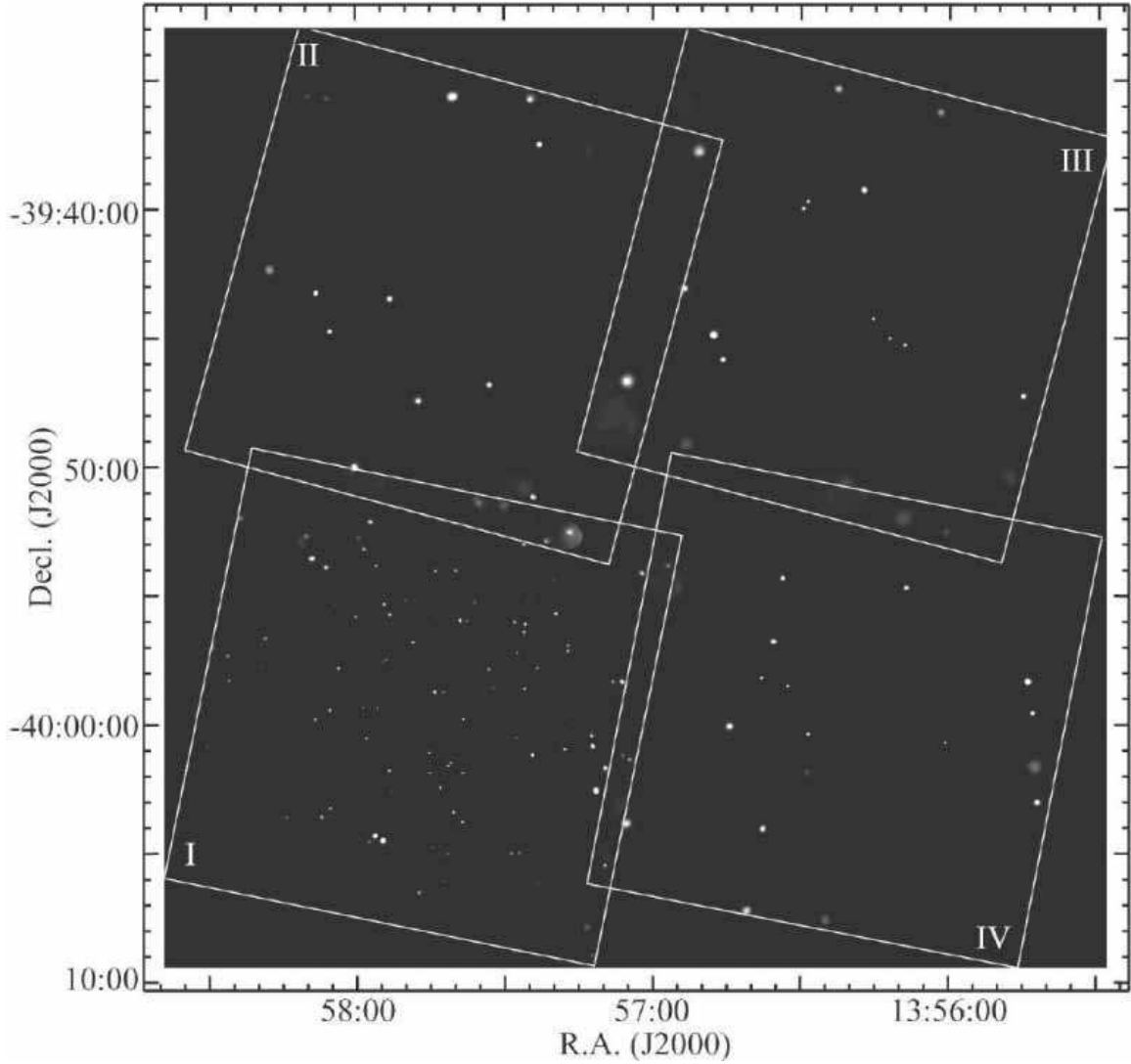


Fig. 3.— Mosaicked and adaptively smoothed *Chandra* ACIS-I image of the CG 12 neighborhood. Smoothing has been performed in the full 0.5 – 8.0 keV band at the 2.5σ level, and gray scales are logarithmic. The four ACIS-I fields are outlined and labelled; most of the 128 X-ray sources can be seen.

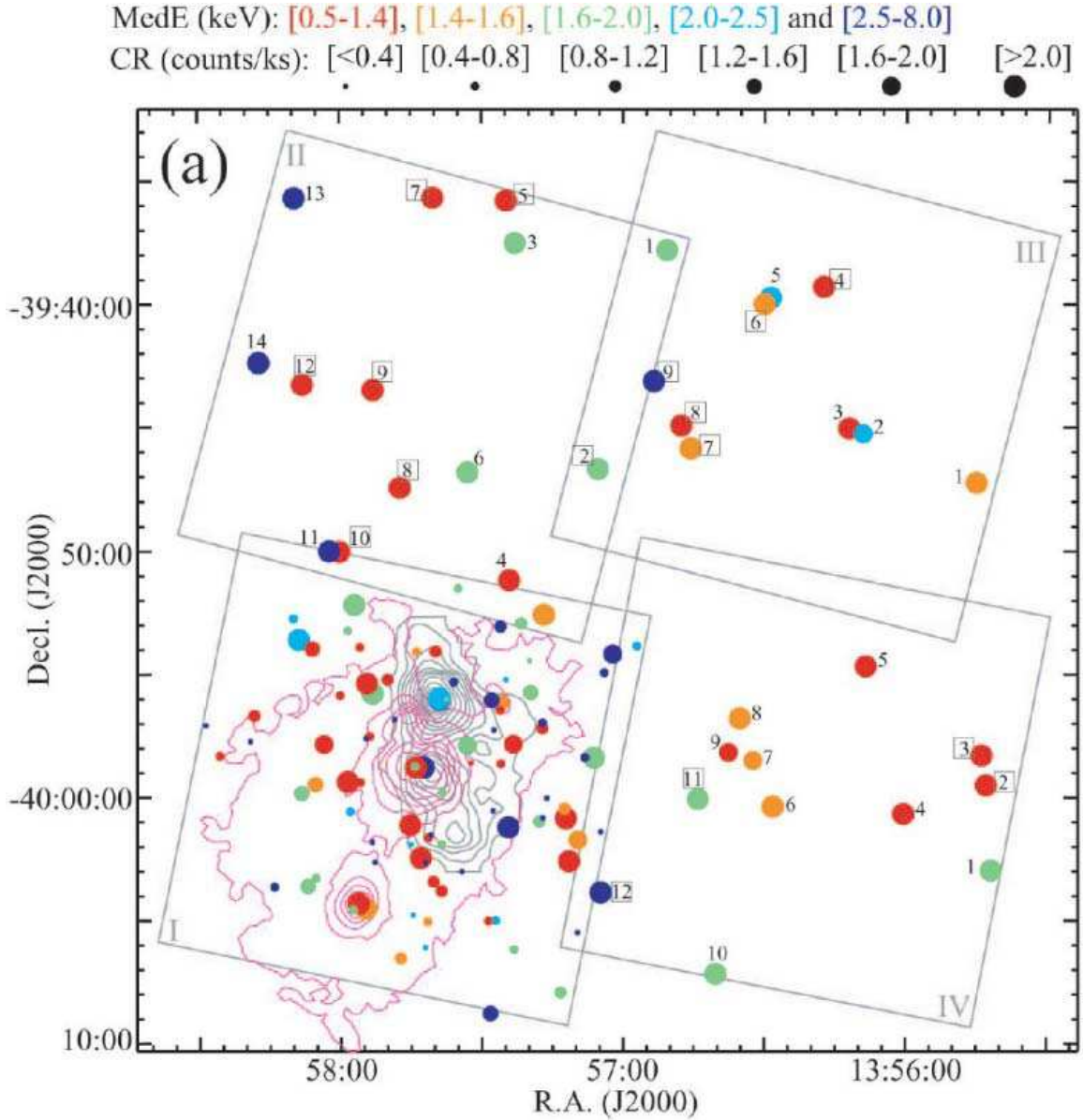
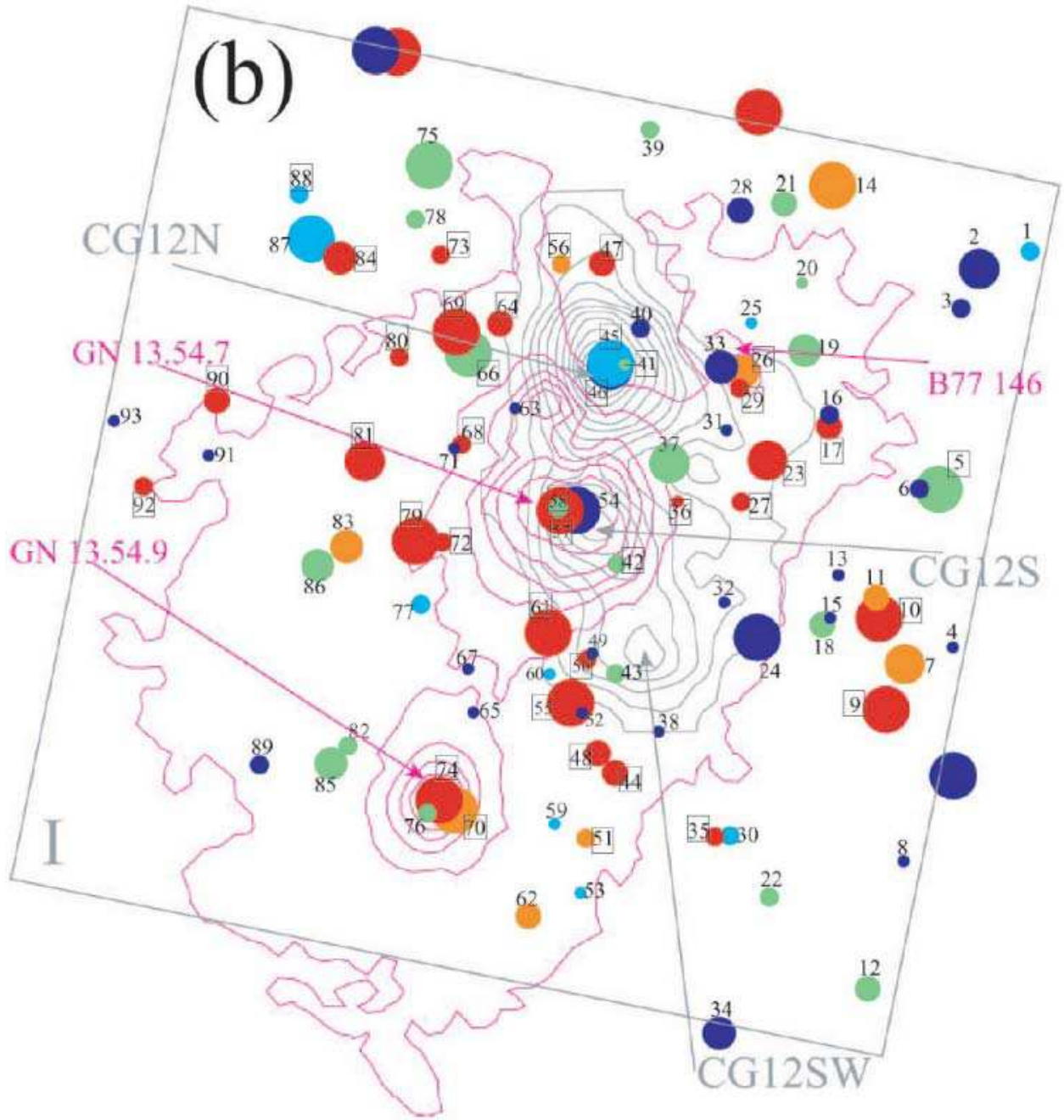


Fig. 4.— Schematic representation of the X-ray source properties in four dimensions: R.A., Decl., median energy, and count rate. The code for symbol colors is given at the top. Symbol size is scaled to source count rate so that weakest sources with $CR < 0.4 \text{ cts s}^{-1}$ are represented by smallest circles and $CR > 2 \text{ cts s}^{-1}$ by the largest circles. The magenta contour outlines the optical nebulae in the head of the globule seen in Figure 1. The grey contour marks the $\text{C}^{18}\text{O}(1-0)$ emission measured by Haikala & Olberg (2006) with contour intervals of 0.3 K km/s which roughly corresponds to 1 mag of visual absorption through the cloud. X-ray sources with ONIR counterparts are outlined by \square ; most of the others are extragalactic contaminants. Panel a: The four *Chandra* fields. Panel b: Close-up view of the primary field. Reflection nebulae are labelled in magenta (Bernes 1977; Neckel & Vehrenberg 1990; Magakian 2003) and molecular cores are labelled in grey (Haikala & Olberg 2006).



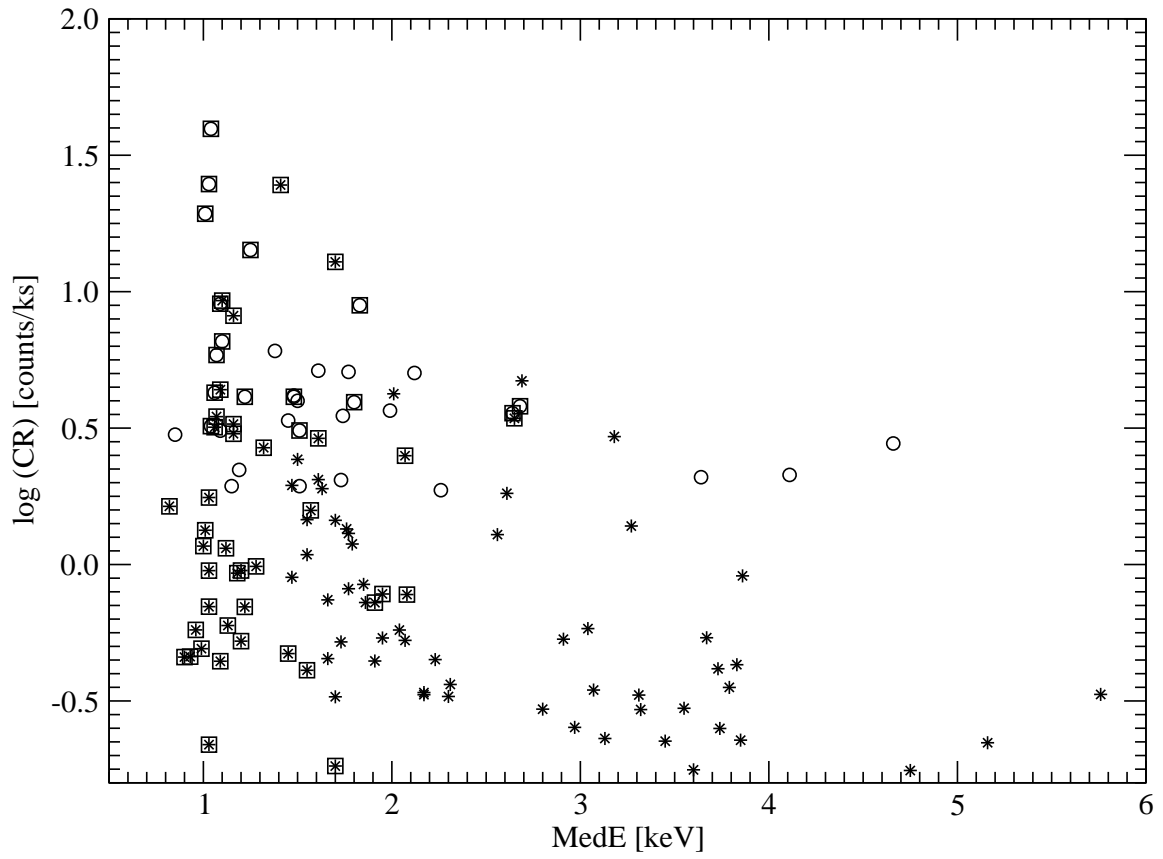


Fig. 5.— X-ray count rate versus X-ray median energy for the 128 *Chandra* sources. Field I sources are represented by star symbols and Field II–IV sources are shown as circles. X-ray sources with optical counterparts are outlined by \square .

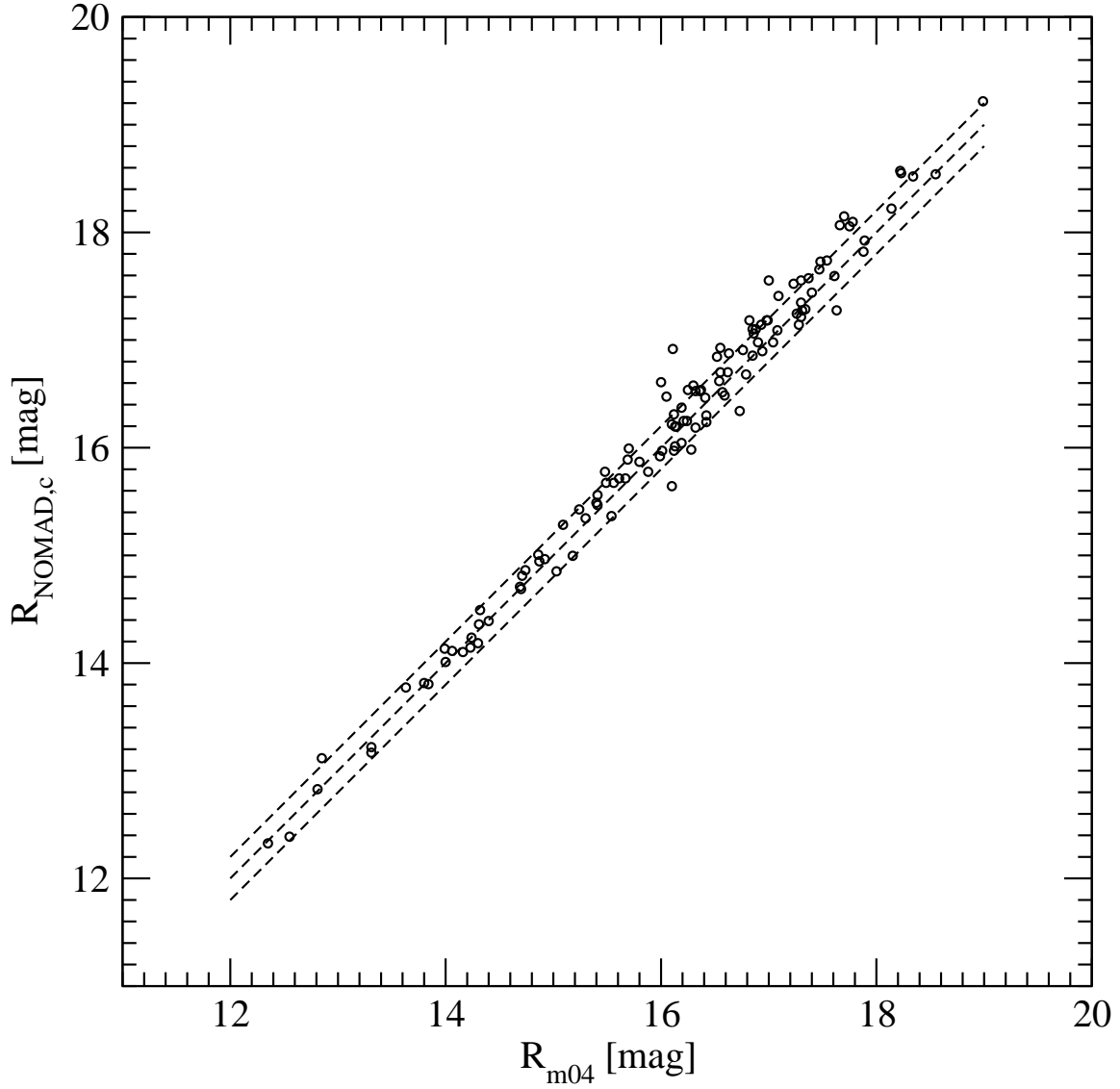


Fig. 6.— Comparison of photographic R -band magnitudes (after linear transformation) with CCD magnitudes for 120 control optical sources lying in the CG 12 field. Dashed lines show $R_{NOMAD,c} - R_{m04}$ values of -0.2, 0, and 0.2.

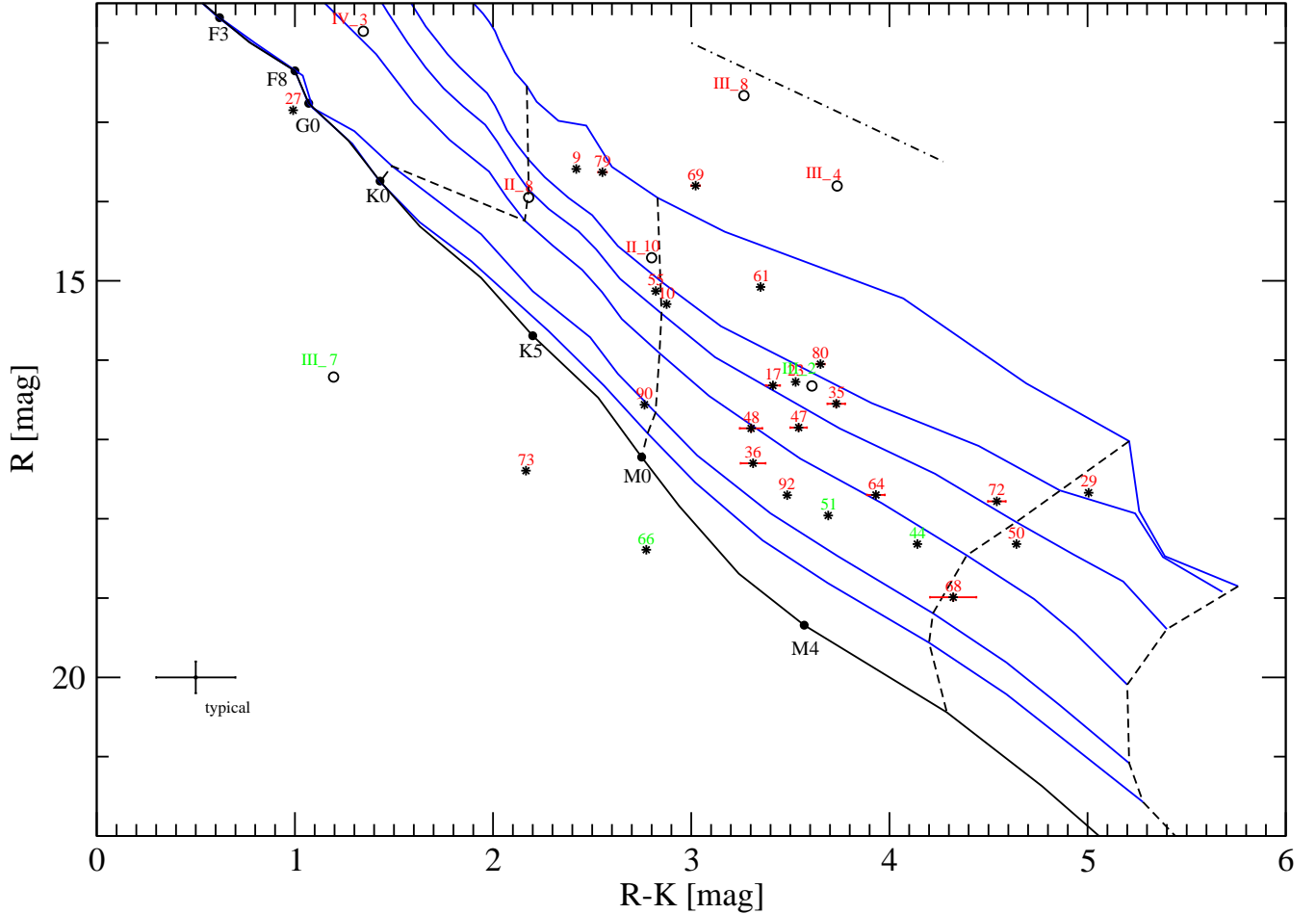


Fig. 7.— R and K band color-magnitude diagram for 32 *Chandra* sources with relatively good photometry. Black stars show sources from Field I and open circles show sources from Fields II–IV. Sources labelled in red are unabsorbed with $MedE \lesssim 1.2$ keV ($A_V \sim 0$ mag), and sources labelled in green are lightly absorbed with $1.3 \lesssim MedE < 1.8$ keV ($A_V \sim 0.5 - 5$ mag). The dashed-dotted line is a reddening vector of $A_V = 2$ mag. The blue solid and dashed black lines, respectively, are PMS evolutionary isochrones for ages 1, 3, 5, 10, 30, 50 Myr, and evolutionary mass tracks for masses 0.1, 0.2, 0.5, and 1.0 M_{\odot} (Siess et al. 2000). The black solid line gives the zero age main sequence locus. A distance of 550 pc to CG 12 is assumed.

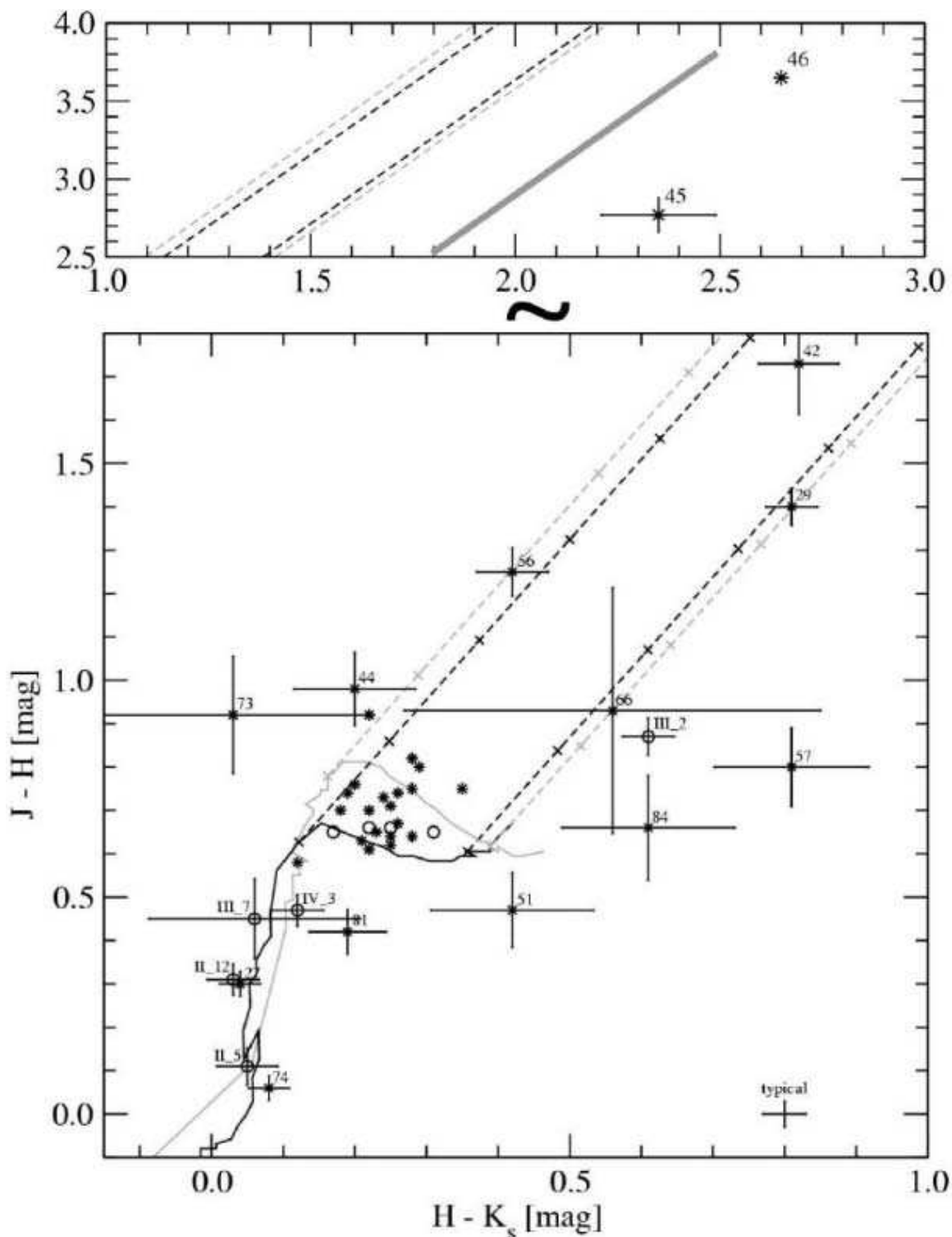


Fig. 8.— JHK_s color-color diagram for 43 *Chandra* sources with reliable NIR photometry. Primary field sources are marked as black stars and secondary field sources as open circles. Sources of special interest or with large errors are labelled. Grey and black solid lines show PMS isochrones transformed to the 2MASS photometric system, for ages 1 and 50 Myr, respectively. Dashed lines are reddening vectors originating from those isochrones at ~ 0.075 and $0.75 M_{\odot}$, marked at intervals of $A_V = 2$ mag. The thick grey line in the upper panel is the rightmost reddening vector for objects from the CTT locus (Meyer et al. 1997).

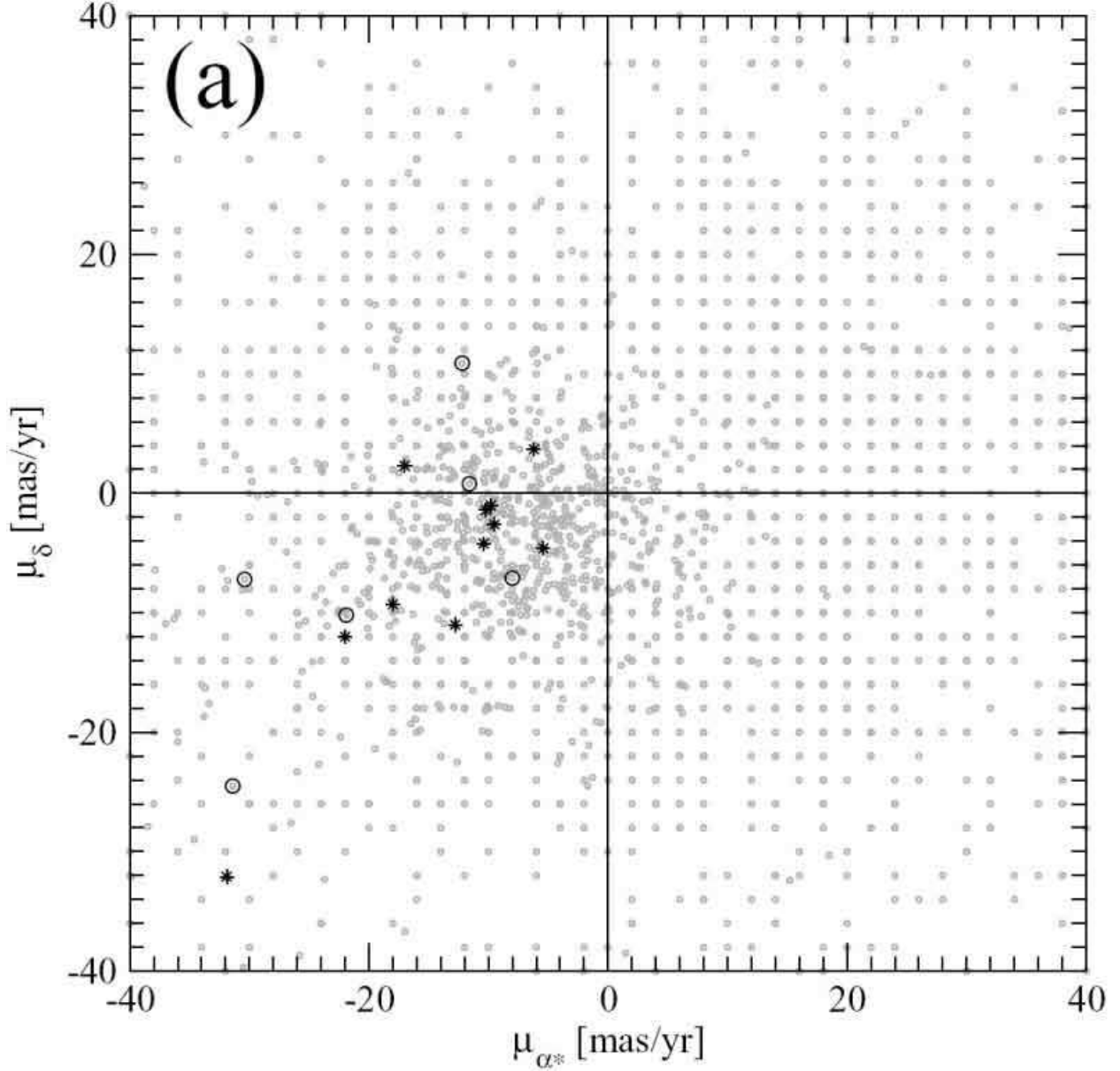
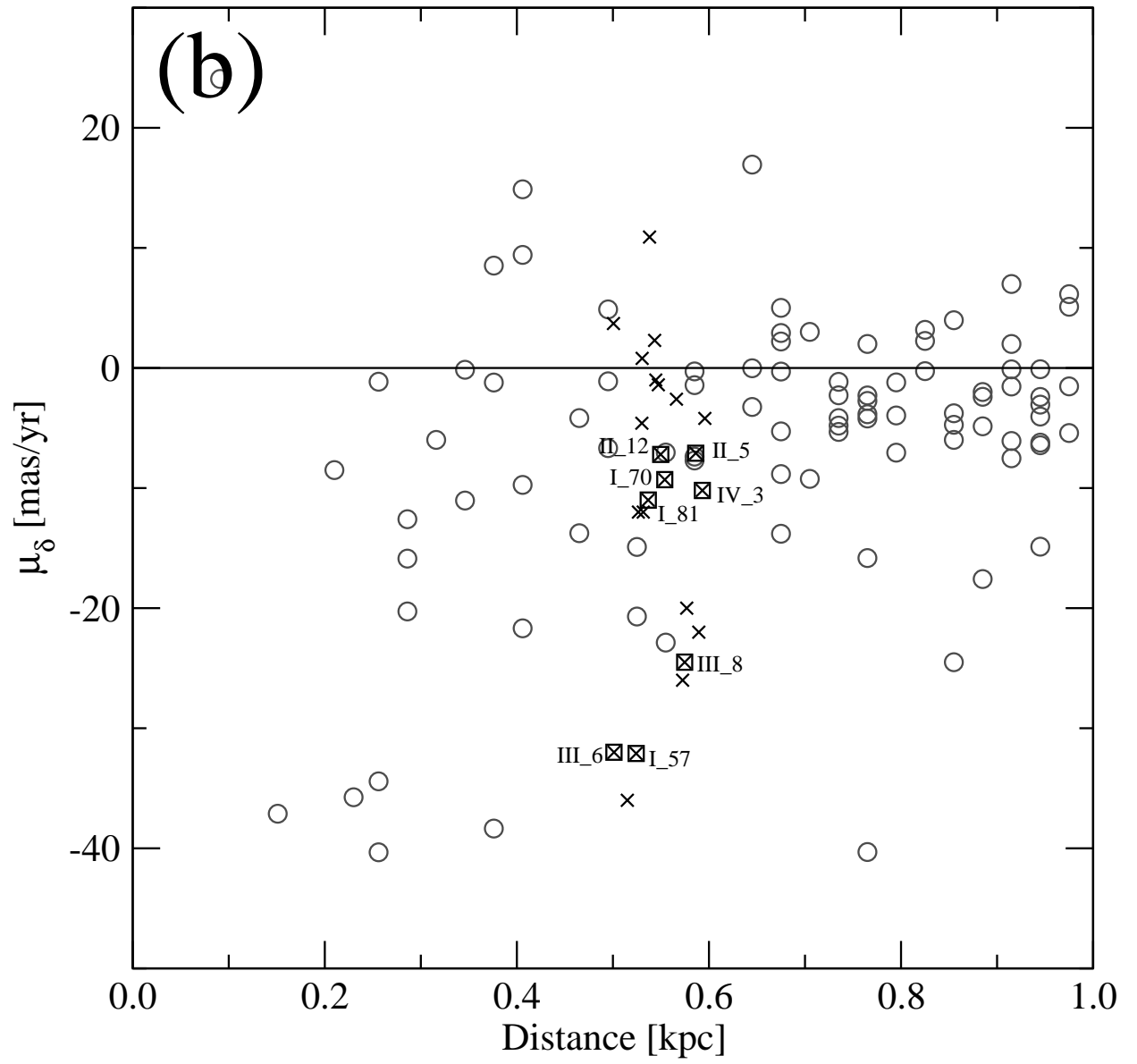


Fig. 9.— (a) Known proper motions from the NOMAD catalog for > 3000 control stars inside the *Chandra* fields (grey circles) and for 17 *Chandra* sources with proper motions known within ± 10 mas yr $^{-1}$ precision (11 from the primary field shown as black *, and 6 from the secondary fields marked by black open o). (b) Proper motions in Decl. for 23 *Chandra* sources (\times) with the eight most reliable values outlined by \square and labelled, and for sources from Besançon model simulated within the distance of 1 kpc from the Sun (grey o). Distances for *Chandra* sources are randomly assigned between 0.5 – 0.6 kpc.



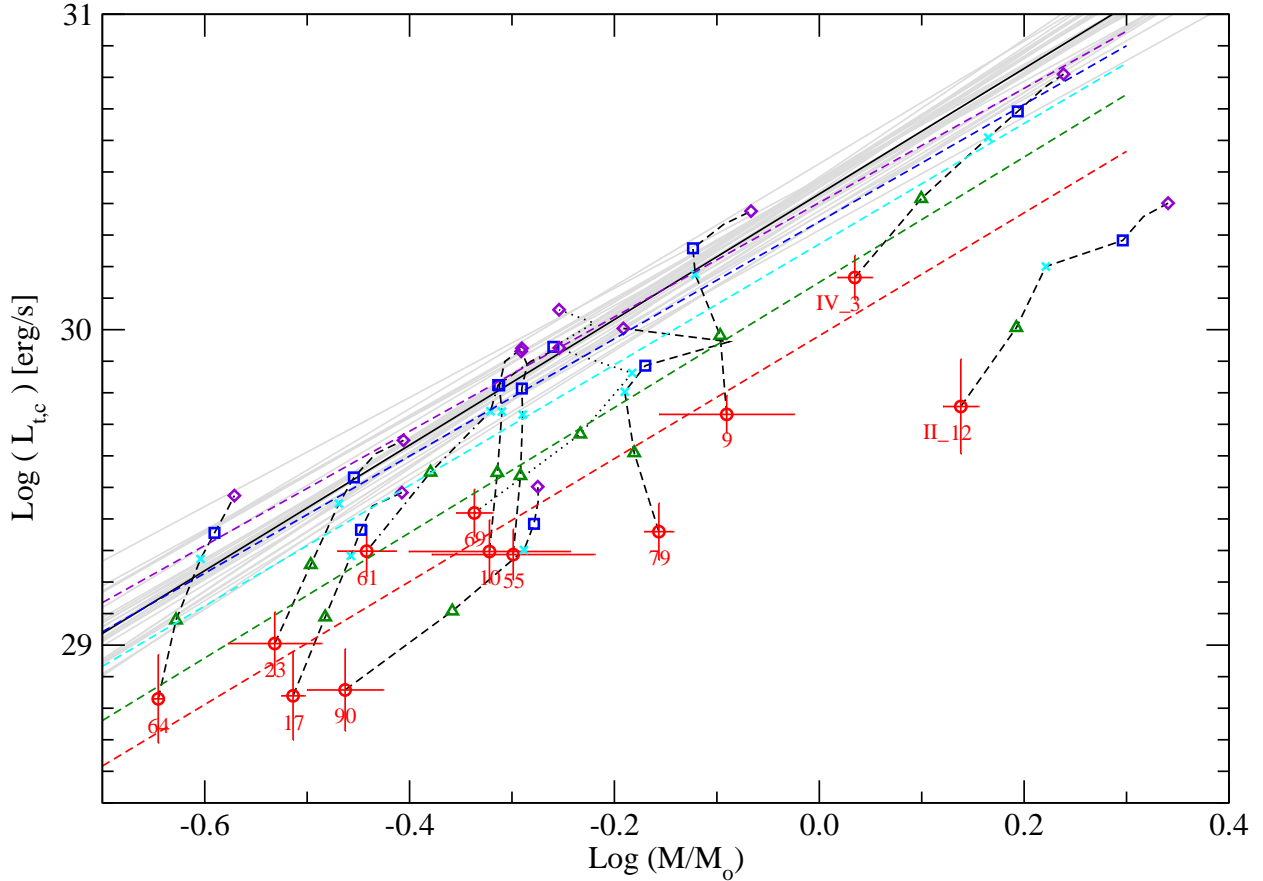


Fig. 10.— X-ray luminosity ($L_{t,c}$) plotted against stellar mass for 12 unobscured X-ray T-Tauri stars, assuming 5 different distances to CG 12: \circ and red line for $d = 300$ pc; \triangle and green line for $d = 400$ pc; \times and cyan line for $d = 500$ pc, \square and blue line for $d = 550$ pc; \diamond and violet line for $d = 630$ pc. Regression lines exclude source #12. Red error bars indicate uncertainties on $\log L_{t,c}$ and $\log M/M_{\odot}$ at $d = 300$ pc, and are similar for other distances. The solid black line is a regression fit for PMS stars in the Orion Nebula Cluster with standard deviation shown by the grey lines.

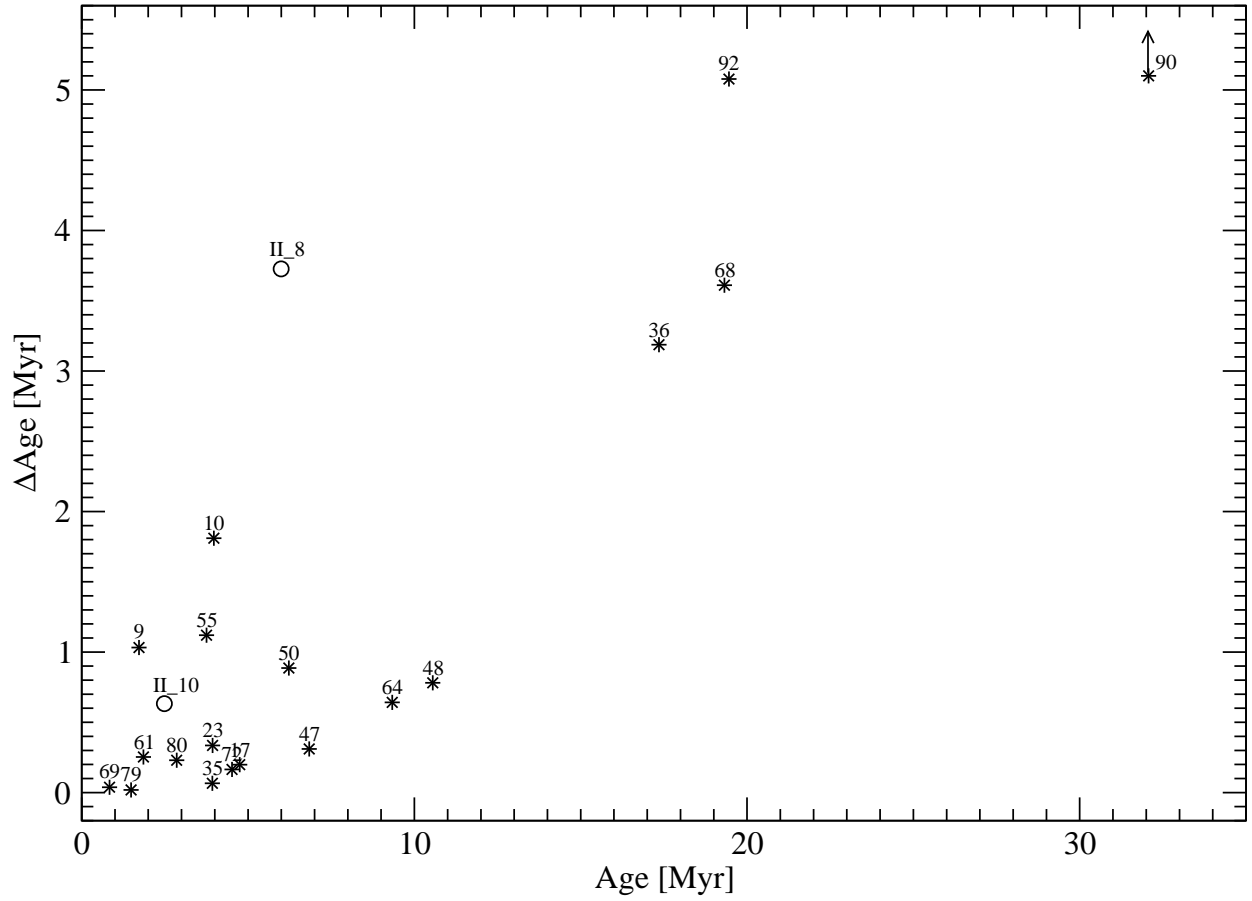


Fig. 11.— Photometric isochronal age estimates and their formal errors for the unobscured population of low-mass X-ray stars in CG 12 for primary field (★) and secondary field (○) sources.

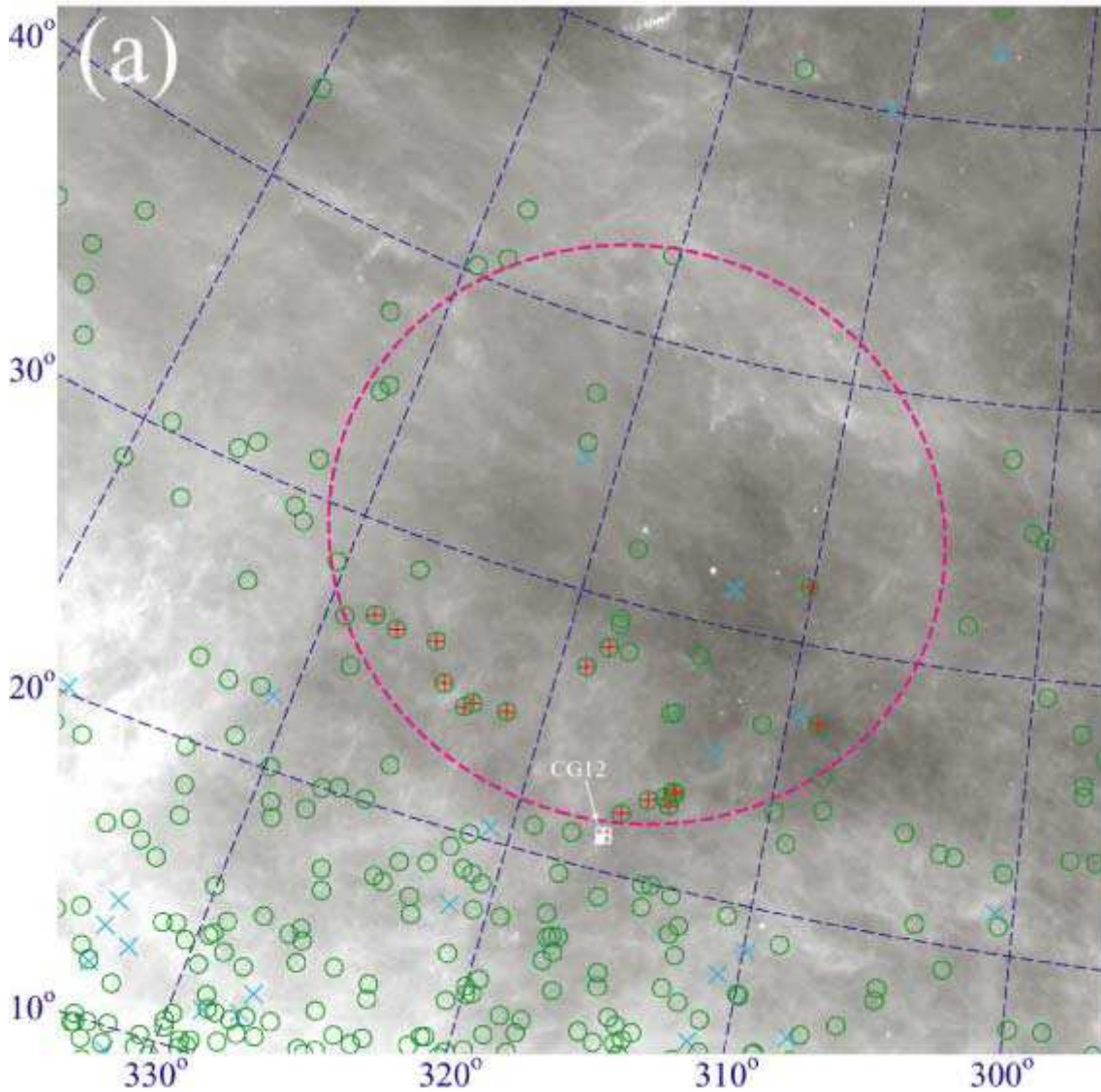


Fig. 12.— (a) IRAS 100 μ m image ($\sim 40^\circ \times 40^\circ$) with the *Chandra* fields marked as small white squares. The wall of the giant IRAS loop GIRL G318 + 32 is marked by the magenta circle. B-type stars from the HD catalog are marked by green circles, and those inside the loop with estimated photometric distances of $350 < d < 700$ pc from the Sun are indicated by red + symbols. Radio pulsars are shown with cyan \times . (b) Close-up view ($\sim 3.5^\circ \times 3.5^\circ$) of CG 12 and a nearby group of B stars from DSS: A – HD 120958, B – HD 120124, C – HD 119627, D – HD 119484, E – HD 119338, and F – HD 119277. The tail axis of the CG 12, marked as white dashed line, passes right through HD 120958.

